

Modelling injection and feedback of Cosmic Rays in grid-based cosmological simulations: effects on cluster outskirts.

F. Vazza^{1,2*}, M.Brüggen¹, C.Gheller³, G. Brunetti²

¹ Jacobs University Bremen, Campus Ring 1, 28759, Bremen, Germany

²INAF/Istituto di Radioastronomia, via Gobetti 101, I-40129 Bologna, Italy

³ Swiss National Supercomputing centre, Via Cantonale, CH-6928 Lugano

Received / Accepted

ABSTRACT

We present a numerical scheme, implemented in the cosmological adaptive mesh refinement code *ENZO*, to model the injection of Cosmic Ray (CR) particles at shocks, their advection and their dynamical feedback on thermal baryonic gas. We give a description of the algorithms and show their tests against analytical and idealized one-dimensional problems. Our implementation is able to track the injection of CR energy, the spatial advection of CR energy and its feedback on the thermal gas in run-time. This method is applied to study CR acceleration and evolution in cosmological volumes, with both fixed and variable mesh resolution. We compare the properties of galaxy clusters with and without CRs, for a sample of high-resolution clusters with different dynamical states. At variance with similar simulations based on Smoothed Particles Hydrodynamics, we report that the inclusion of CR feedback in our method decreases the central gas density in clusters, thus reducing the X-ray and Sunyaev-Zeldovich effect from the clusters centre, while enhancing the gas density and its related observables near the virial radius.

Key words: galaxy: clusters, general – methods: numerical – intergalactic medium – large-scale structure of Universe

1 INTRODUCTION

Galaxy clusters form through the hierarchical assembly of dark matter (DM) and gas over cosmological times. This process happens via super-sonic accretion, with efficient driving of turbulent motions, shock waves and magnetic field compression and amplification in the cosmic gas (e.g. Bykov et al. 2000; Dolag et al. 2008; Brüggen et al. 2011, and references therein). This picture is based on observational evidences (e.g. Carilli & Taylor 2002; Govoni et al. 2002; Ferrari et al. 2008, for recent results), and is theoretically supported by numerical simulations (e.g. Ryu et al. 1998; Dolag et al. 1999; Miniati et al. 2000, 2001; Ryu et al. 2003; Pfrommer et al. 2007; Iapichino & Niemeyer 2008; Hoeft et al. 2008; Kang et al. 2007; Skillman et al. 2008; Vazza et al. 2009; Donnert et al. 2009; Vazza et al. 2009, 2011a; Bonafede et al. 2011). However, the details of the interplay between various non-thermal components of the ICM are still quite uncertain.

Shock waves driven by the accretion of matter constitute the most important channel for the thermalization of baryonic gas over cosmological time, and they may also be efficient sites of cosmic ray particles (CR) acceleration. CRs are thought to be accelerated in the pattern of MHD fluctuations across the shock transition, in a process known as diffusive shock acceleration, DSA

(e.g. Bell 1978; Blandford & Ostriker 1978; Drury & Voelk 1981; Ellison et al. 1995; Kang & Jones 1990; Malkov & O’C Drury 2001; Kang & Jones 2007; Kang et al. 2009; Caprioli et al. 2010). The diffusion of accelerated particles across the shock produces a shock-precursor, which modifies the overall compression produced by the entire shock structure in a non-linear way (e.g. Drury & Voelk 1981; Blasi 2004; Amato & Blasi 2005). The main factors which govern the overall efficiency of the injection of relativistic particles are the Mach number of the shock, M , and the properties of the magnetic field in the shock transition. At quasi parallel shocks, M is the primary parameter which determines the acceleration efficiency of CRs, while the secondary parameter is the minimum momentum of injection of particles, p_{th} , required to start the acceleration. In the test-particle regime, where the accelerated particles do not have any dynamical feedback on the structure of the shock, the DSA predicts the universal energy spectrum of $N(p)dp \propto p^{-q}dp$ for the accelerated particles, where q is related to the Mach number only via $q = 2(M^2 + 1)/(M^2 - 1)$. However, models of DSA predict that at strong shocks, $M > 5$, the fraction of accelerated CR particles becomes non-negligible compared to the thermal pool, $\xi > 10^{-3}$, and that a significant fraction of the shock energy is transferred to the CR particles, which in turn modify the shock structure. The result is a larger shock compression and an amplification of the magnetic fields in the pre-shock region (e.g Kang et al. 2009, for a modern review). The basic predictions of

* E-mail: f.vazza@jacobs-university.de

DSA have been tested successfully with multi-band observations of radio and γ emission from remnants of supernovae (e.g. Reynolds 2008; Vink et al. 2010; Edmon et al. 2011).

Once accelerated, CR particles can accumulate in galaxy clusters (Berezinsky et al. 1997; Völk & Atoyan 1999) possibly producing an important non-thermal component which could be directly sampled by future gamma ray observations (e.g. Pinzke & Pfrommer 2010; Brunetti & Lazarian 2011a). Secondary particles injected in the ICM via proton–proton collisions may cause detectable synchrotron radiation (e.g Blasi & Colafrancesco 1999; Dolag & Enßlin 2000) and, as well as primary particles, that are re-accelerated by MHD turbulence and may thus escape radio halos (Brunetti et al. 2008). CR particles can mix with the thermal plasma, and may have an important dynamical effect on the ICM (e.g. Ruszkowski & Oh 2011; Brunetti & Lazarian 2011b). Its role can also be that of shaping the evolution of X-ray cavities powered by AGN jets (e.g. Mathews & Brightenti 2007; Guo & Oh 2008; Mathews & Guo 2011), and to provide an additional source of thermalization in cool core clusters, via Alfvén wave dissipation (e.g. Guo & Oh 2008).

The goal of this work is to provide a simplified but robust algorithm to model the run-time injection of CR particles at cosmological shock waves, their advection and their dynamical effect on the evolution of thermal gas in large-scale structures. This complements the methods developed by Pfrommer et al. (2007) and Enßlin et al. (2007), where the injection and feedback from CRs is simulated with Lagrangian cosmological simulations using smoothed-particle-hydrodynamics. To this end, we implemented new modules to follow CRs in the framework of the public 1.5 version of the *ENZO* code (Bryan et al. 1995), and we run a number of validation tests and large-scale production runs in cosmology.

The paper is organized as follows: in Sect.2 we describe the algorithms developed to treat the injection, advection and dynamical feedback of CRs in *ENZO*; in Sect.3 we present one-dimensional tests for the code and its various options; in Sect.4 we present our 3-D results in cosmology, obtained with fixed mesh resolution (Sect.4.1) and adaptive mesh refinement (Sect.4.2). A discussion of the results is given in Sect.5, while our conclusion are summarized in Sect.6.

2 NUMERICAL METHODS

2.1 ENZO 1.5

All simulations in this work were performed using the *ENZO 1.5* code developed by the Laboratory for Computational Astrophysics at the University of California in San Diego (<http://lca.ucsd.edu>).

ENZO is an adaptive mesh refinement (AMR) cosmological hybrid code highly optimized for high performance computing (Bryan et al. 1995; O’Shea et al. 2004; Norman et al. 2007; Collins et al. 2010). It uses a particle-mesh N-body method (PM) to follow the dynamics of the collision-less Dark Matter (DM) component (Hockney & Eastwood 1988), and an adaptive mesh method for ideal fluid-dynamics (Berger & Colella 1989).

The DM component is coupled to the baryonic matter (gas) via gravitational forces, calculated from the total mass distribution (DM+gas) solving the Poisson equation with an FFT based approach. The gas component is described as a perfect fluid and its dynamics is calculated by solving conservation equations of mass, energy and momentum over a computational mesh, using an Eulerian solver based on the Piecewise Parabolic Method (PPM,

Colella & Woodward 1984). This scheme is a higher-order extension of Godunov’s shock capturing method (Godunov et al. 1976), and it is at least second-order accurate in space (up to the fourth-order in 1-D, in the case of smooth flows and small time-steps) and second-order accurate in time.

For a more detailed overview of the numerical algorithms in *ENZO* and of the updated strategies for handling the data-structures in the simulations, we refer the readers to the excellent recent review of Collins et al. (2010).

2.2 Shock identification

We follow the standard assumption of Diffusive Shock Acceleration, relating the injection efficiency of Cosmic Rays at shocks to the Mach number of the shock (e.g. Kang & Jones 2007, and references therein).

In order to model the injection of CRs at shock waves, a reliable on-the-fly method to measure the Mach number of shocks in the simulation is required.

A few grid-based methods in the literature were tested in recent years that apply the Rankine-Hugoniot jumps conditions across shocked cells (e.g. Miniati et al. 2000; Ryu et al. 2003; Skillman et al. 2008; Vazza et al. 2009).

In our algorithm, we detect and measure the Mach number of shock waves during run-time using an approach based on the differences of the gas pressure (or gas plus CR) between cells. This method is conceptually very similar to the “Temperature Jump” method of (Ryu et al. 2003) and to the “Velocity Jump” method of Vazza et al. (2009). We decided, however, to use pressure as main variable of the method, since the CRs pressure is also the physical quantity used in the code (see Sec.2.3.3 for a discussion).

Our code first selects candidate shocked cells by requiring that the flow in the cell is converging: $\nabla \cdot \mathbf{v} < 0$. Then the 3-D distribution of cells around the candidate cell is analysed with one-dimensional scans along the three axes, and it is checked that the gas temperature, T , and the gas pseudo-entropy, $S = P \cdot \rho^{-\gamma}$ (where ρ is the gas density and γ is the adiabatic index) change in the same direction, $\nabla S \cdot \nabla T > 0$ (e.g. Ryu et al. 2003).

The gradient of temperature then sets the candidate post-shock and pre-shock cells. The Mach number is then evaluated from the information of the pressure jump between cells given by the Rankine-Hugoniot condition:

$$\frac{P_2}{P_1} = \frac{2\gamma M^2 - \gamma + 1}{\gamma + 1}, \quad (1)$$

where P_2 (P_1) is the gas pressure where the temperature across the candidate cells is the highest (the smallest). By construction, we consider pre-shock and post-shock cells with a stencil of 3 cells around the minimum of the 3-D divergence.

In the case of candidate shocked cells with several Mach numbers along the different axes, and in case of multiple candidate shocked cells along the same direction, we “clean” the preliminary map of Mach numbers by retaining only the maximum Mach number provided by the algorithm, for the considered patch of cells (e.g. Ryu et al. 2003). Obliquity in shocks can also lead to a small additional smoothing of the shock transition across a few cells (e.g. Tasker et al. 2008; Skillman et al. 2008). We verified that in the case of oblique shocks in 3-D, the Mach number reconstructed by our procedure is equal, within a $\sim 5 - 10$ percent even for strong shocks, to that measured for perpendicular shocks having the same input Mach number. Given our cleaning procedure on multiple shocked cells along the same scan direction, our code also

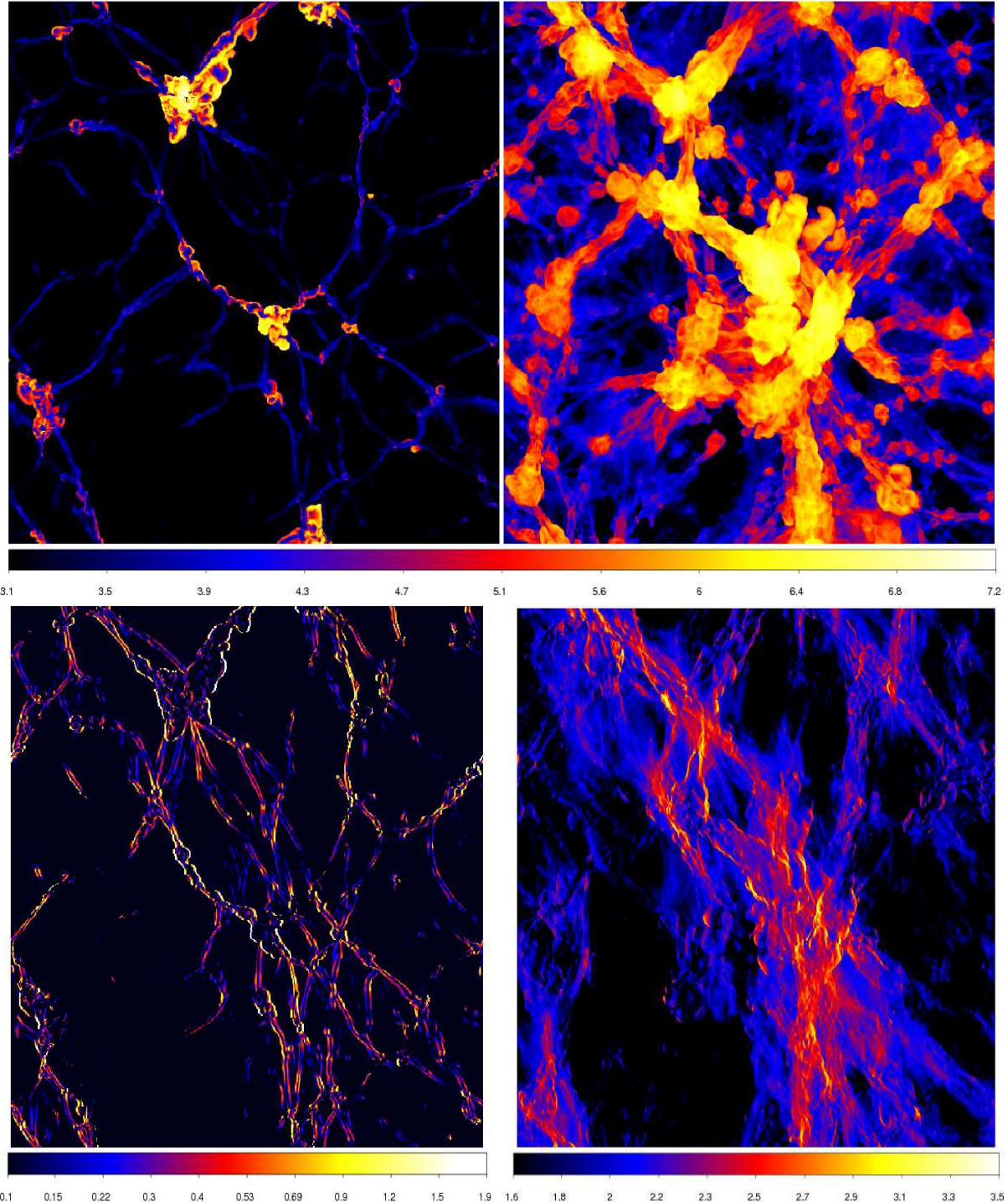


Figure 1. 2-dimensional slice showing $\log_{10}(T)$ (top panels, in units of [K]) and $\log_{10}(M)$ reconstructed in run-time by our code (bottom panels), for the full simulated cubic volume with the side of 80 Mpc at 512^3 at $z = 0$. The left panels show the maps for a slice of depth 300 kpc, while the right panels show the (volume-weighted) projected maps for a line of sight of 20 Mpc.

makes sure that the reconstructed pattern of shocks, which is used for the injection of CR energy, is always 1 cell thick (see the first two maps of Fig.3).

Based on our tests (Vazza et al. 2009), the use of a stencil of ~ 3 cells ensures in general the best reconstruction of the shock jumps in cosmological runs. Also, this avoids the contamination of density/temperature fluctuations associated to substructures in

clusters (e.g. small gas clumps) when the Mach number is computed. Usually, only very strong shocks ($M \gg 10$) are spread across more than 3 cells in cosmological simulations, so only in these cases we underestimate M slightly. However, these shocks are very rare and not relevant for the production of CR energy in clusters (e.g. Ryu et al. 2003; Pfrommer et al. 2006; Skillman et al. 2008; Vazza et al. 2009). Given the shape of the acceleration effi-

ciency we use here (see Sect.2.3.1 and Fig.4), the exact value of shock strength is not crucial for $M > 20 - 30$, since the assumed efficiency function saturates for very strong shocks.

Figure 1 shows the results of our run-time detection scheme for a cosmological box of 80 Mpc simulated with a fixed grid resolution (Run1_h in Tab.3.3, $\Delta x = 156$ kpc). We show volume-weighted maps of gas temperature (top panels) and of Mach number reconstructed at run-time by our algorithm (bottom panels) for a thin slice of 300 kpc (left panels) and for a much larger slice with the thickness of 20 Mpc (right panels). Similar to what is found in other papers (e.g. Miniati et al. 2001; Ryu et al. 2003; Skillman et al. 2008; Vazza et al. 2009), the outer regions of clusters and filaments are surrounded by strong, $M \gg 10$, regular patterns of shocks, while the hotter innermost regions are crossed by more irregular and weaker shocks. Even when seen in projection along a large simulated volume (right panels), our reconstructed shocks trace sharp surfaces surrounding galaxy clusters and filaments, representing efficient and well-confined sites for the injection of CRs inside large-scale structures. We remark that this is already at variance with cosmological SPH simulations, where the outer shocks are much smoother due to the large smoothing length outside large-scale structures (Pfrommer et al. 2007; Hoeft et al. 2008; Vazza et al. 2011b).

In previous work, we demonstrated that an algorithm based on velocity jumps (VJ) between cells may present small advantages in the reconstruction of shock waves outside of clusters, owing to a smaller scatter associated with velocity-based measurements compared to temperature-based measurements (Vazza et al. 2009). However, the vectorial analysis of the 3-D velocity field and the "cleaning" algorithms associated with the procedure, requires a substantially greater amount of calculations compared to scalar-based methods. This is not an issue for any post-processing analysis of shock waves, but it makes a significant difference in performance when the computation is performed in run-time (due to 3-D loops and high memory usage). For this reason, we considered a pressure-based method a good compromise for the run-time use needed here.

In Fig.2 we show the differential volume distribution of Mach numbers for the full simulated cosmological volume, measured with the two methods. The distributions of shocks are divided according to the cosmic environment, depending on the total matter over density of shocked cells, $\delta_\rho \equiv \rho_{\text{tot}}/\rho_{\text{cr}}$ (where ρ is the total gas+DM density and $\rho_{\text{cr}} \approx 9.31 \cdot 10^{-30} \text{ g/cm}^3$ is the critical density of the Universe: voids, $\delta_\rho < 3$, filaments, $3 \leq \delta_\rho < 30$, and galaxy clusters and their outskirts, $\delta_\rho \geq 30$, as in Vazza et al. 2009).

The distributions are very similar to what has been found in our previous work based on fixed resolution simulations in ENZO (e.g. Vazza et al. 2011b). At the scale of galaxy clusters outskirts and galaxy clusters virial volumes ($\delta_\rho > 30$) the two methods yield nearly identical results.

In runs where adaptive mesh refinement (AMR) is turned on, the Mach number is computed at all refinement levels, using a stencil of cells at the same level. The Mach number estimated at the highest resolution is always preferred in the case of several Mach numbers for the same cells, obtained with different AMR levels. In this paper, we employ adaptive mesh refinement using the criteria outlined in Vazza et al. (2009). This means that an AMR criterion based on velocity jumps in 1-D is added to the usual criteria of gas and DM over density (e.g. O'Shea et al. 2004), ensuring that

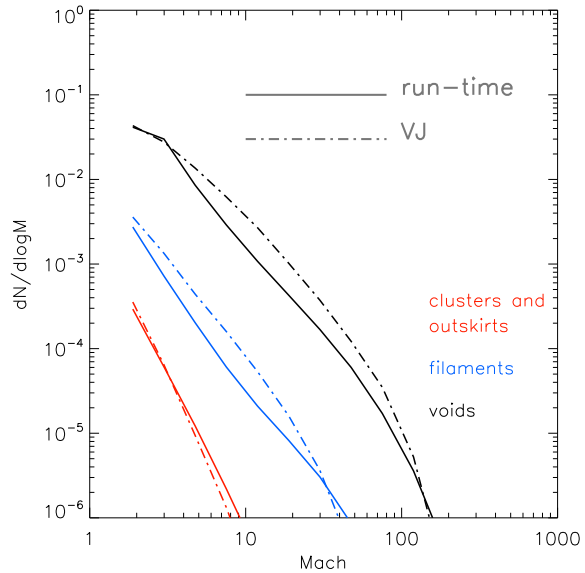


Figure 2. Volume distribution of Mach numbers in a simulated cosmological box of side 80 Mpc (Run1_h, see Table 3.3). The solid lines report the results for the run-time shock finder employed in this work, the dot-dashed lines are for the velocity jumps method introduced in Vazza et al. (2009), run over the same data. The different colours show the results for different cosmic environments.

virtually *all* shocks with ($M > 2$) within the AMR regions are re-sampled down to the maximum available resolution. Hence, almost the entire population of shocks contributing to CR acceleration (Sect.2.3.1) is reconstructed and measured using the highest available resolution in the domain. Figure 3 shows the pattern of Mach numbers reconstructed in run-time by our method (left panel) for a galaxy cluster. It also shows the energy flux of CRs and the gas energy for a run employing 5 levels of mesh refinement (the slice has a side length of ~ 5 Mpc and a depth along the line of sight of 32 kpc).

In the case of a mixture of gas and CRs, the total Mach number of the shocks can be obtained by Eq.1, provided that the total pressure and an effective adiabatic index (as $\gamma_{\text{eff}} = (\gamma P_g + \gamma_{\text{cr}} P_{\text{cr}})/(P_g + P_{\text{cr}})$, Enßlin et al. 2007, where $\gamma_{\text{cr}} = 4/3$).

2.3 Method for Cosmic Rays

In the following sections we describe our numerical implementation of the injection, the spatial advection and the pressure feedback of CRs.

In this work, we consider only CR *protons*, for which to first approximation radiative and Coulomb losses and the inelastic proton-proton collisions can be neglected, for the time-scales of interest here (e.g. Miniati 2007). The extension to CR electrons and the modelling of radiative, Coulomb losses and proton-proton collisions for both species will be investigated in future work. Also, we only consider CRs generated at large-scale structures shocks. The inclusion of other sources of CRs, such as supernovae or AGN, as well as the coupling of our method for CRs to the new MHD version of ENZO (Collins et al. 2010) will also be the subject of future work.

In summary, in our implementation we inject the energy of CR particles at shocks during run-time assuming Diffusive Shock

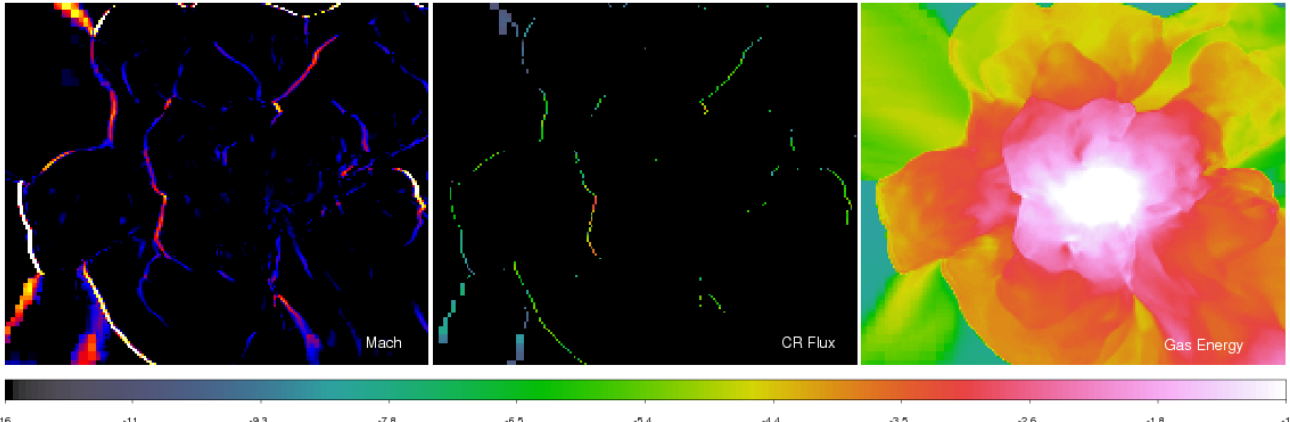


Figure 3. 2-dimensional slices showing the Mach number (left, color coding as in the bottom left panel of Fig.1), the energy injected into CR during the last time step (central panel, in $\log_{10}[\text{codeunits}]$) and gas energy (same color coding of central panel) for a slice with side of $\sim 5 \text{ Mpc}$ along a line of sight of 32 kpc. The simulation employs nested initial conditions and 5 levels of mesh refinement. The fact that only cells with $M > 2$ are used for the injection of CRs, explain the small difference in morphologies between the left and the central panel in the Figure (see Sec.2.3.1 for details).

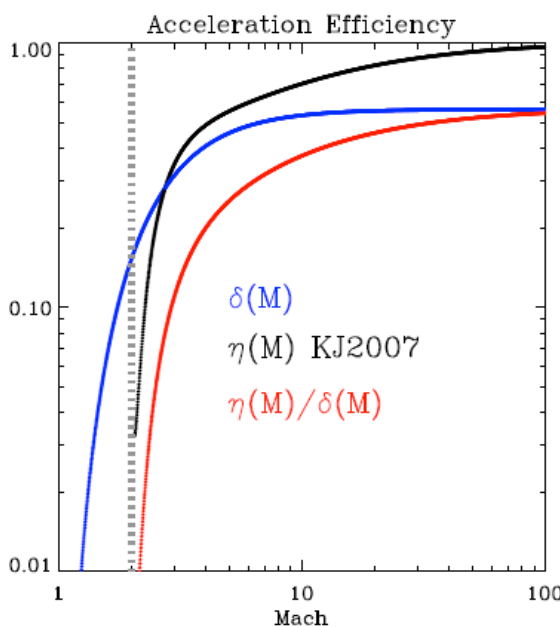


Figure 4. Trend with the Mach number of the acceleration efficiency at shocks for the (Kang & Jones 2007) efficiency ($\eta(M)$, in red), for the standard thermalization efficiency in the post-shock ($\delta(M)$, in blue) and for the ratio of the two (black). In this plot, the kinetic energy flux across the surface of the shock is normalized to one.

Acceleration (2.3.1), we remove this energy from the thermal gas energy pool (2.3.2), we advect it in the simulated volume along with the thermal gas energy (2.3.3), and we compute its pressure feedback by adding to the total pressure (2.3.4). In order to preserve numerical stability, new time stepping criteria are added to the standard ones (Sec.2.3.5).

2.3.1 The injection of Cosmic Rays

In our treatment of DSA, we rely on the results of numerical, mostly one-dimensional studies of CR acceleration at shock waves as a function of background plasma parameters (e.g.

Malkov & O'C Drury 2001; Kang & Jones 2007; Kang et al. 2009; Caprioli et al. 2010)

The injection of CR energy in 1-D quasi parallel shocks has been studied in detail with advection-diffusion equations for a variety of shocks, for velocities in the range $150 \leq v_s \leq 4500 \text{ km/s}$ and for pre-shock temperatures of $10^4 - 10^6 \text{ K}$. In these models the partial dissipation of shock kinetic energy into the excitation of Alfvén modes is accounted for, while in our treatment we neglect the presence of pre-existing CR energy in computing the injection of new CR energy. This is clearly a limitation of our treatment. However, self-consistent recipes to compute the estimated acceleration efficiency as a function of both the shock Mach number and the ratio of CR energy to gas thermal energy at every shock are presently unavailable, since they require the full self-consistent solution of diffusion-convection equations (e.g. Kang & Jones 2007; Caprioli et al. 2010).

Based on these theoretical papers, we assume that a small fraction of the incoming protons is instantly accelerated at the dissipative gas sub-shock to a speed larger than the post-shock sound speed, and that it contributes to the CR pressure inside the cell.

For every detected shock we compute the co-moving shock speed $v_s = Mc_s$ and the resulting energy flux of accelerated CR protons, as a function of the Mach number:

$$\phi_{\text{cr}} = \eta(M) \cdot \frac{\rho_u v_s^3}{2} = \eta(M) \cdot \frac{\rho_u c_s^3 M^3}{2}, \quad (2)$$

where ρ_u is the co-moving up-stream gas density and $\eta(M)$ is a function of M , whose numerical approximation can be found in Kang et al. (2007). For simplicity we restrict the acceleration of CRs to $M \geq 2$, given that the acceleration of CRs for very weak shocks is expected to be extremely small, and it is still very poorly constrained (Kang & Ryu 2010). The trend with Mach number of $\eta(M)$ in the Kang & Jones (2007) model is shown in Fig.4, along with the trend of the standard thermalization efficiency from Rankine-Hugoniot jump conditions ($\delta(M)$) and the ratio between the two.

To obtain the injected energy density of CRs within each cell, we integrate the CR energy flux over the time step:

$$e_{\text{cr}} = \frac{\phi_{\text{cr}}}{\rho} \cdot \frac{dt_1}{dx_1}, \quad (3)$$

where ρ is gas density in the cell, dx_1 is the cell size at the refinement level 1 and dt_1 is the time step of the simulation at that refinement level. The CR energy density, e_{cr} , is therefore our main variable to simulate the evolution and dynamics of relativistic particles in the two-fluid model, and it represents the integrated energy density over the energy/momentum spectra of the CR distribution, $e_{\text{cr}} \propto \int E \cdot N(p) dp \propto \int p^4 \cdot f(p) \cdot (1 + p^2)^{-1/2} dp$.

In every cell, the contributions of the CR energy fluxes from all directions are added, and the CR energy at the various AMR level is handled as all other primary quantities in *ENZO* (see Collins et al. 2010, for a review).

2.3.2 Reduced thermalization at shocks

The transfer of energy from the thermal gas to CRs causes a reduced thermalization efficiency in the post-shock region (e.g. Amato & Blasi 2005). This effect can be modelled by removing the corresponding energy flux of accelerated CR from the post-shock region, thus ensuring energy conservation where Eq.3 is applied.

In *ENZO*, the "dual energy formalism" (Ryu et al. 1993; Bryan et al. 1995) is used, which means that whenever the internal gas energy, e_g , cannot be calculated correctly as the difference between total, $e_{\text{tot}} = e_g + v^2/2$ (where v is the modulus of the velocity field), and kinetic energy (due to the fact that $e_{\text{tot}} \gg e_g$ in highly supersonic flows, and that there round-off errors dominate) the total energy is evolved. Since the acceleration of CR affects the thermalization efficiency of post-shock regions, we need to update the two energies in a consistent way. Once e_{cr} has been computed (Eq.3), we update the values of the total energy and of the gas internal energy within the cell according to: $e'_g = e_g - e_{\text{cr}}$ and $e'_{\text{tot}} = e_{\text{tot}} - e_{\text{cr}}$. This step is performed before starting the Riemann solver of the PPM method at the following time step. In cosmological runs without heating from the re-ionization field (e.g. Haardt & Madau 1996), the temperature of the background gas can reach un-realistically low temperatures, $T < 10$ K, with extremely strong shocks ($M > 1000$, Vazza et al. 2009). In these cases, one may end up in the situation of having $e_g - e_{\text{cr}} < 0$ in some cells, due to similar round-off errors as in the estimate of e_g . Considering that this problem arises only in extremely rarefied regions and in the absence of a re-ionization background, we just fixed it by forcing our version of *ENZO* not to inject new CRs if this is going to produce negative values of e_g or e_{tot} . This fix has no consequence on all thermal and non-thermal statistics of our simulated large-scale structures, and this problem does not arise when realistic models for background radiation from re-ionization are adopted.

2.3.3 Spatial advection of CR energy

Once injected, the CRs are spatially advected assuming they are "frozen" into the gas velocity field. This follows from neglecting the effect of the spatial diffusion of CRs during the simulation.

Run-time processing of spatial diffusion of CRs is computationally expensive, and requires the knowledge of the \vec{B} field topology and of MHD modes in the simulated volume. However, according to quasi-linear theory, the spatial diffusion is not expected to play a role for the physical scales we study here, $L > 25 - 100$ kpc, given that the typical diffusion time of \sim GeV particles in the ICM is of the order of $\sim 1 - 10$ Gyr for scales of $L \sim 100$ kpc assuming $B \sim 0.1 - 1 \mu\text{G}$ (e.g. Blasi et al. 2007, as a recent review). Since the bulk of CR energy is injected at $z \leq 1$ (Sect.4.1), the effect of spatial diffusion is small compared to the typical scales analysed in

our simulations, $\sim 100 - 1000$ kpc. However, the distributions of CRs can be slightly modified by the action of diffusion, which may smooth our distributions on $L_{\text{diff}} \sim 50 - 100$ kpc. Since the self-consistent inclusion of diffusion (and conduction) processes in the simulated ICM is still challenging (e.g. Ruszkowski et al. 2011), and since a self-consistent magnetic field is not included in our version of *ENZO*, we consider the above as an unavoidable limitation of our present method.

No other dynamical exchange between CRs and thermal gas is assumed to take place (e.g. Coulomb losses), and the coupling between CRs and baryonic gas proceeds via the momentum equation (see below).

The energy of CRs is advected in space by solving:

$$\frac{\partial E_{\text{cr}}}{\partial t} + \nabla \cdot (E_{\text{cr}} \mathbf{v}) + P_{\text{cr}} \cdot \nabla \cdot \mathbf{v} = 0, \quad (4)$$

where $E_{\text{cr}} = \rho e_{\text{cr}}$, and where we assume a *constant* pseudo-adiabatic index for the CR energy (e.g. Kang & Jones 1990; Mathews & Guo 2011). Consequently, cosmic ray pressure, P_{cr} , and energy, e_{cr} , are related via

$$P_{\text{cr}} = (\gamma_{\text{cr}} - 1)\rho e_{\text{cr}} = (\gamma_{\text{cr}} - 1)E_{\text{cr}}. \quad (5)$$

Equation 4 is numerically solved as:

$$E_{\text{cr},i}^{n+1} = E_{\text{cr},i}^n + dt/dx[(E_{\text{cr},i-1/2}^{n+1/2} \cdot v_{i-1/2}^{n+1/2} - E_{\text{cr},i+1/2}^{n+1/2} \cdot v_{i+1/2}^{n+1/2}) + P_{\text{cr}}^* \cdot (v_{i-1/2}^{n+1/2} - v_{i+1/2}^{n+1/2})],$$

where

$$P_{\text{cr}}^* = \frac{\gamma_{\text{cr}} - 1}{2} \cdot (E_{\text{cr},i-1/2}^n + E_{\text{cr},i+1/2}^n) \quad (6)$$

is the "centred" CR pressure between the two faces of the cell (e.g. Bryan et al. 1995).

Equation 6 is computed similarly to the total energy and internal energy equations in *ENZO*, via one-dimensional sweeps along each direction and using the information of the fluxes, $v_{i-1/2}^n$ and $v_{i+1/2}^n$, reconstructed by the PPM method (e.g. Bryan et al. 1995).

The effects of cosmological expansion on CRs is treated separately, by updating the CR energy density, e_{cr} :

$$\frac{\partial e_{\text{cr}}}{\partial t} = -3 \frac{(\gamma_{\text{cr}} - 1)\dot{a}}{a} e_{\text{cr}}, \quad (7)$$

where a and \dot{a} are the cosmological scale factor, and the scale factor rate of change at each time step (e.g. Bryan et al. 1995).

The real value of the CR adiabatic index

$$\gamma_{\text{cr}}^* = \left| \frac{d \log P_{\text{cr}}}{d \log \rho} \right| \quad (8)$$

cannot be derived self-consistently, since this would require the knowledge of the distribution of the CR momenta, $f(p)$. Depending on the shape of the momentum distribution and of the minimum momenta, q_{\min} , this may range from $\gamma_{\text{cr}}^* = 4/3$ to $\gamma_{\text{cr}}^* = 5/3$ (e.g. Ensslin et al. 2007). In numerical simulations of DSA, where the diffusion-convection equation for the evolution of the $f(p)$ is solved in run-time, and coupled to the dynamical equation of the gas evolution (e.g. Kang & Jones 2002), the adiabatic index can be computed self-consistently. In our case, the value of $\gamma_{\text{cr}}^* = \gamma_{\text{cr}}$ can only be assumed a-priori. In the following, we will produce tests and simulations where we fix the adiabatic index to its most extreme value of $\gamma_{\text{cr}} = 4/3$.

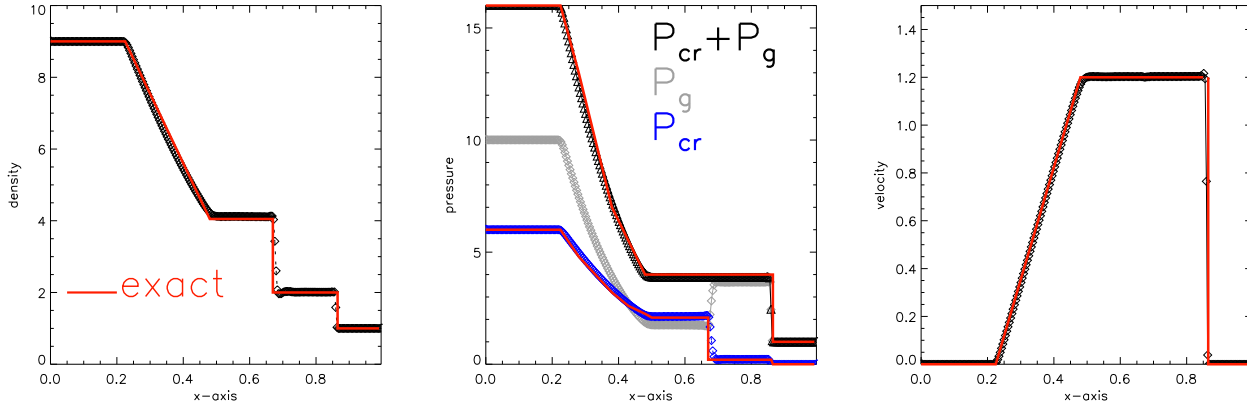


Figure 5. Shock tube test for $P_{\text{cr},1} = 6$, $P_{g,1} = 10$ and $\rho_1 = 9$, and assuming an acceleration efficiency of $\eta \approx 0.05$ at the shock front. The left panel shows the profile of gas density, the central one the profiles of P_g , P_{cr} and P_{tot} , while the right one shows the profile of velocity. The diamonds represent the solution for our code, while the solid red lines shows the numerical solution obtained by Miniati (2007).

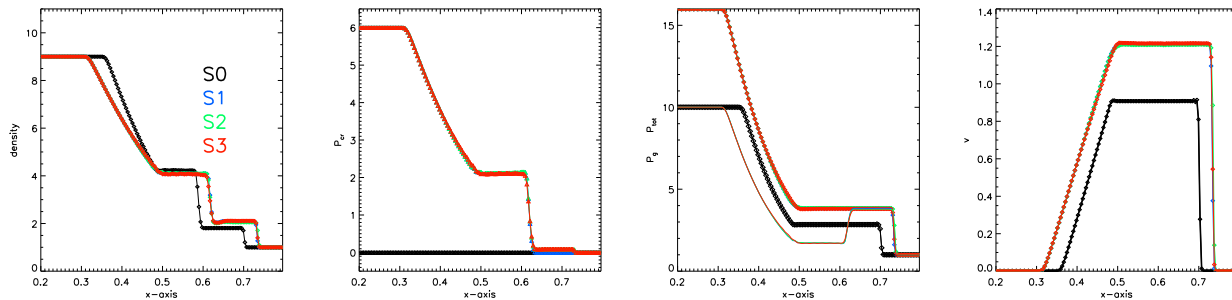


Figure 6. Shock tube test for the various physical modules available to our method. From left to right, we show: gas density, CR pressure, total (thick lines) and gas (thin lines) pressure, velocity field. The initial conditions are as in Fig.5, and $\eta = 0.02$ is assumed at the shock front.

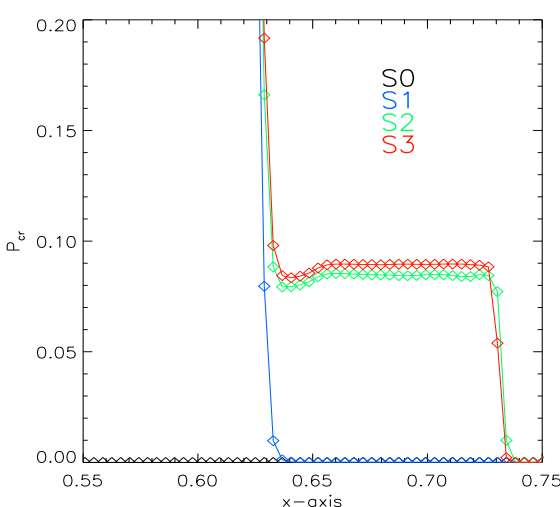


Figure 7. Zoomed version of Fig.6 for the CR pressure at the shock front. The meaning of colours is as in Fig.6.

2.3.4 Dynamical feedback of CR

The dynamical coupling between CRs and the thermal gas is done by updating the gas pressure with the total pressure from the mix-

ture of gas and CRs within every cell. At each time step, the total thermal gas pressure, $P_g = \rho(\gamma - 1)e_g$ (with $\gamma = 5/3$) is replaced with the effective pressure in the cell, $P_{\text{eff}} = P_g + P_{\text{cr}}$, where P_{cr} is given in Eq.5.

The effective pressure P_{eff} is then fed to the Riemann solver in the next time step, and the new "left" and "right" states around each cells are reconstructed based on the new effective pressure. The momentum equation from these states is then solved in the usual way in ENZO, and the resulting velocity field is used to update the evolution of all gas quantities in the simulation, as well as of CRs energy field, E_{cr} (Eq.4).

In order to achieve numerical solutions without spurious oscillations, it is crucial that all fluxes associated with the total pressure, P_{eff} , and with the CR pressure, P_{cr} , fed into the Riemann solver are passed through the same slope limiters in order to keep the sharpness of solutions around shocks and in strong rarefaction regions (e.g. Colella & Woodward 1984; Bryan et al. 1995). Our tests suggests that this is particularly important when the energy density of CRs is of the order of $e_{\text{cr}} \sim 0.1e_g$, or larger.

Furthermore, when the "left" and "right" edge states of the Riemann problem are computed for the solution of the fluxes, the appropriate wave velocity is used; this implies replacing $c_s = \sqrt{\gamma P_g / \rho}$ with

$$c'_s = \sqrt{\frac{\gamma P_g + \gamma_{\text{cr}} P_{\text{cr}}}{\rho}} \quad (9)$$

in the associated routines of the PPM algorithm, as suggested in Miniati (2007).

2.3.5 Time stepping

To ensure numerical stability in the presence of feedback from CRs, we implement 2 additional constraints on the time stepping criteria of *ENZO* (see Collins et al. 2010, for a review).

First, we modify the Courant condition on the hydrodynamical time step by replacing the standard speed of sound with c'_s (as defined in Eq.9):

$$\Delta t = \min\left(\frac{dx_1}{c'_s \pm v}\right), \quad (10)$$

where v is the 1-dimensional gas velocity along one axis, and the minimum is taken over the stencil of cells at each refinement level. We need also to ensure that the internal energy correction (see Sec.2.3.3), due to the reduced thermalization process, is not larger than a fraction of the gas energy within the cell, since this would cause numerical instabilities. We achieve this by imposing:

$$\Delta t_{\text{cr}} \leq \epsilon_{\text{cr}} \cdot e_g \cdot \frac{\Delta_1}{\phi_{\text{cr}}}, \quad (11)$$

which follows from the requirement that $\epsilon_{\text{cr}} e_g \geq e_{\text{cr}}$ at each cell. Our tests suggest that $\epsilon_{\text{cr}} = 0.02 - 0.04$ is a suitable choice to ensure that the modification of the thermal energy in the post-shock is not dramatic during each time step, also in the case of the complex 3-D flows (which may cause fluxes of accelerated CRs across several faces of a cell). Compared to the standard cosmological simulations at fixed grid resolution, the use of these additional time stepping criteria usually produce an increase of ~ 15 percent in the total CPU time by the end of runs.

3 TESTS IN ONE DIMENSION.

3.1 Shock Tube with pre-existing Cosmic Rays

We performed one-dimensional shock tube tests assuming a mixture of CRs and thermal gas in the initial setup, and investigating the behaviour of our scheme at different Mach numbers.

The parameters of the first shock tube test are identical to those reported in Miniati (2007): the initial left state is filled with a mixture of gas and CRs, with pressure (in code units) $P_{g,1} = 10$, $P_{\text{cr},1} = 6$, and density $\rho_1 = 9$, while all the fields on the right state are set to 1 ($\gamma_{\text{cr}} = 4/3$ is assumed everywhere for CRs).

In Fig.5 we show the comparison of our test with the numerical solution of Miniati (2007), at approximately the same epoch. In this case, all physical modules in our version of *ENZO* with Cosmic Rays are activated: advection, injection, pressure feedback and reduced thermalization at the post-shock. The agreement of our run with the results of Miniati (2007) is excellent, with a constant total pressure level in the post-shock region. The contact discontinuity at the rarefaction wave is reconstructed in a few cells (which is common in the PPM method), while the transition of the shock is reconstructed in ~ 2 cells.

The numerical implementation of our CR code also allows us to investigate the role of each physical module separately. We show the effect of each module in Fig.6, where the same initial conditions of the previous shock tube were re-simulated by modelling: only the advection of CRs is modelled (run *S0*); the advection of CRs and their pressure feedback onto the gas component (*S1*); the

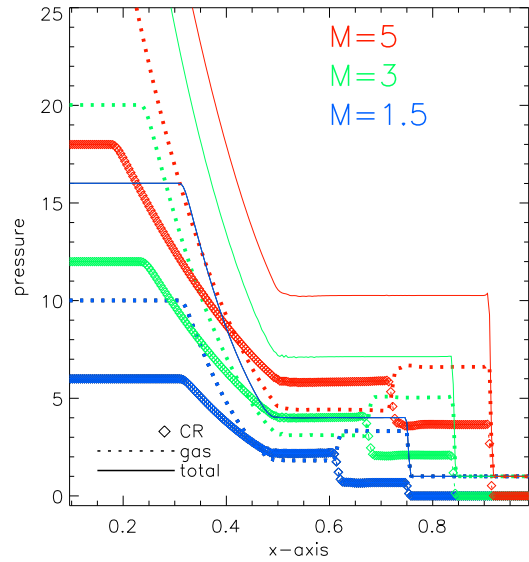


Figure 8. Behaviour of the gas pressure (dots), CR pressure (diamonds) and total pressure (solid lines) for shock tube tests leading to a $M \approx 1.5$ (blue), $M \approx 3$ (green) and $M \approx 5$ (red) shocks. Only the values of CR pressure are shown for clarity; the x-axis is in units of the total box length.

injection of new CR energy at the shock (*S2*); the whole set of CR modules (*S3*).

When we allow CRs to have pressure feedback on the gas (*S1*), the total pressure of the system is increased and the behaviour of gas density, velocity and of the total pressure are scaled-up versions of those in *S0*. However, the behaviour of gas pressure at the shock front is modified by the presence of the CR pressure. The injection of CR energy at the shock front in *S2* (here $\eta \approx 0.03$) slightly increases the total pressure at the shock compared to *S1*. When including the reduced thermalization (*S3*), the total pressure at the shock front is smaller compared to *S2*, and as a result the speed of the shock front is decreased. Figure 7 shows a close-up of the behaviour of CR pressure at the shock front. Only very small oscillations (at the percent level) are present in the post-shock solution of our CR fluid.

In all runs where the CRs are allowed to exert a pressure on the gas (*S1*, *S2* and *S3*), the solution in the rarefaction region does not vary. This confirms that the treatment of CR acceleration at the shock does not affect any other region in the shock tube.

In a second set of shock tube tests, we varied the initial conditions by increasing the gas pressure on the left side in order to produce stronger shocks. In Fig.8 we show the results for shock tubes leading to $M \approx 1.5, 3$ and 5 and assuming $\eta \approx 0.3$ to highlight the effect of CR injection at the shock. Even for the strongest shock, the post-shock total pressure shows no significant spurious oscillation, and the shock edge is still reconstructed in 2-3 cells at most.

3.2 Shock Tube without pre-existing Cosmic Rays

Next, we focus on the injection of CR energy at the shock front by simulating similar 1-D shock tubes as in the previous case, but assuming no pre-existing CR energy at the beginning of the simulation. Also, we increased the values of initial gas pressure on the left side of the box ($P_{g,1} = 10, 20, 30, 60$ and 120). In these tests, we let

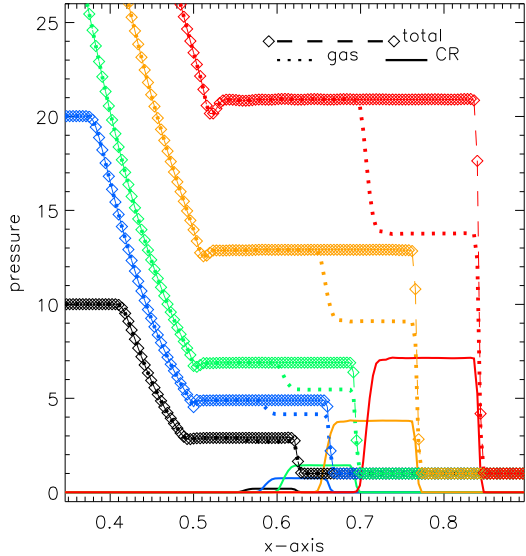


Figure 9. Behaviour of the gas pressure (dots), CR pressure (diamonds) and total pressure (solid lines) for several shock tube tests without pre-existing CR energy. Only the cell-wise values for the total pressure are shown for clarity.

$\eta(M)$ vary with the shock Mach number according to the model of Kang & Jones (2007), which we will use in our cosmological runs.

The results are shown in Fig.9. At the strongest shocks, the freshly injected CR pressure becomes comparable to the post-shock gas pressure ($P_{\text{cr}} \sim 0.3P_g$). The total pressure behind the shock still remains constant, despite a small amount of oscillations of numerical nature. Again, the shock edge is reconstructed within 2-3 cells at most in all tests.

To avoid any smoothing of the shock region, which may cause spurious effects when the non-linearity of CR acceleration schemes is coupled to the system, Miniati (2007) proposed the application of a hybrid Godunov-Glimm's scheme to ensure the sharpest reconstruction of shocks in the simulation.

In order to limit the effect of a broadened shock profile on the estimate of the injected CR energy in all our tests here and in the production runs (Sec.4), our run-time shock finder (Sec.2.2) measures Mach numbers in the simulations across 3 cells. This was motivated by our previous work on cosmological shock waves in ENZO simulations (Vazza, Brunetti & Gheller 2009), where we studied the best stencil of cells needed to correctly capture shock waves in the PPM version of ENZO. With this approach, the effect of numerical smearing of reconstructed shocks only has a very limited impact on the estimated injection efficiency of CRs, since M is always measured with a stencil of cells close to the (small) numerical smearing of shocks in the PPM method.

3.3 Zeldovich Pancake

In order to test our implementation of cosmic ray physics in a simple cosmological framework, we run a set of Zeldovich Pancake test and compare the results with and without the dynamical role of CR energy injected at shocks. The initial conditions ($z_i = 50$ in our case) for this test assume a purely baryonic Universe, with a uniform initial pressure and density, and a converging velocity field with $v = 0$ at the centre of the domain. With this setup we

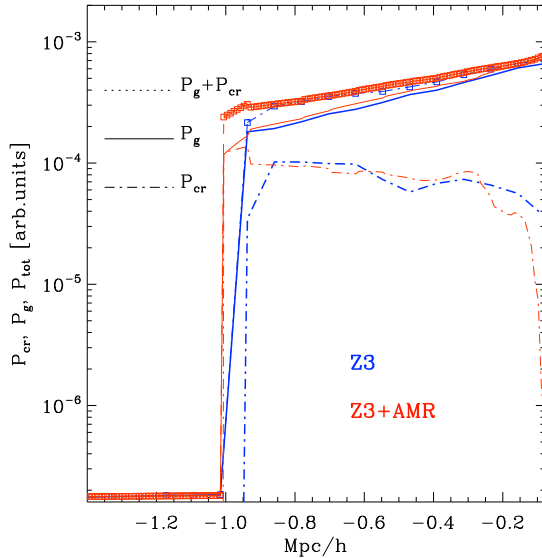


Figure 11. Comparison of the total pressure of the Zeldovich collapse test in Z3 employing fixed resolution and of the Z3 with 4 levels of AMR. The different lines show: gas pressure (solid), CR pressure (dot-dashed) and the total pressure (dotted).

simulate the evolution of a co-moving box of $L_{\text{box}} = 20$ Mpc/h ($h = 0.72$) with a grid of 256 cells. No CR energy is present in the box at the start of the simulation. Here results are presented for the simple collapse test (run Z1), and for the full set of physical modules for CRs (Z3). In all cases the acceleration efficiency is the one of Kang & Jones (2007). Additionally, in order to test the reliability of our method with adaptive mesh refinement, an AMR run with a 16 times higher spatial resolution has been performed (run Z3+AMR).

The panels in Figure 10 show the evolution of gas density, gas pressure, CR pressure, total pressure and total energy in runs Z1 and Z3. By the end of the runs the profile of the "pancake" is very similar in all cases, with sizable differences at the percent level which are evident for $z < 2$, after enough CR energy has been injected by the expanding shocks. The gas density and gas pressure of Z3 are slightly smaller inside the structure and slightly larger in the external regions (at $\sim -0.8 - 1.2$ Mpc/h), while the total pressure profile is very similar in the two cases, with the exception of the outer region where run Z3 shows an excess. The reason for this behaviour is that, when output at equal times is compared in runs Z1 and Z3, the outer shocks in the simulation with CRs are found to have expanded to a slightly larger distance, due to their enhanced total pressure. The combination of the softer equation of state of the gas+CR composite adopted in Z3 at the outer regions, and the total larger pressure jumps felt by the gas accreted onto the pancake makes this mechanism very stable, since both effects concur to have a more efficient injection of CRs in the system, due to the increase of the Mach number of external shocks. We will discuss this mechanism again in Sec.4 and in the Appendix, with the results of fully cosmological runs in 3 dimensions.

By the end of this run, the pressure ratio between CRs and gas is $P_{\text{cr}}/P_g \sim 0.6$ at the external regions and $P_{\text{cr}}/P_g \sim 0.05 - 0.1$ in the innermost region of the pancake.

In Fig.11 we show the effect of AMR (4 levels of refinement, triggered by the local gas overdensity) on the same collapse test.

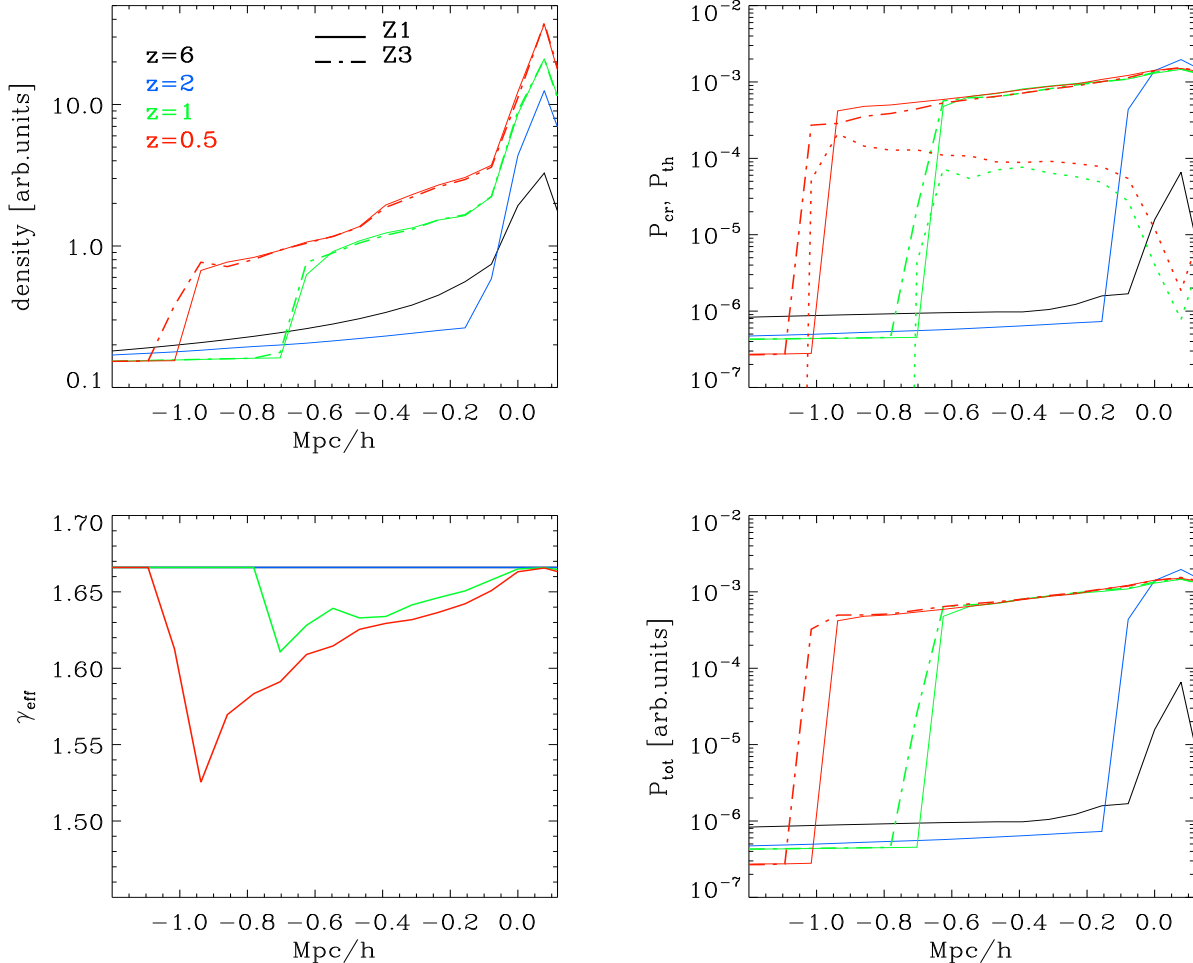


Figure 10. Time evolution of the profiles of gas density, gas and CR pressure (dotted lines in the second panel), effective adiabatic index (bottom left) and total pressure (bottom right) for the Zeldovich collapse test run with no CR physics (solid lines, run Z1) and with CR physics (dot-dash, run Z3).

The solution recovered by the end of the run is quite similar to Z3, provided that the larger spatial resolution here enables a sharper modelling of the outer shock, and leads to a larger injection of CRs. These two effects modify the shock speed in a non-linear way, making the synchronization of the two runs not trivial. The energy ratio measured at the outer region is larger compared to Z3, yielding $P_{\text{cr}}/P_g \sim 0.5$. Based on the profile of P_g and P_{cr} along the pancake, we conclude that the previous results at coarser resolution are stable against such a dramatic increase of resolution, even if the detailed distribution of P_{cr} at the shock edge may slightly vary with resolution. As in the previous case, this difference can be partially ascribed to small timing issues in the comparison of the two runs, and partially to the slightly enhanced amount of CRs injection measured at higher resolution.

4 RESULTS IN COSMOLOGICAL SIMULATIONS

We produced a large set of cosmological simulations in order to study the evolution of CRs accelerated at accretion shocks in large-scale structures, and their dynamical feedback on the clustering properties of the thermal baryon gas. In a first set of simulations,

we studied the large-scale properties of CRs using fixed grid simulations (Sect. 4.1), while in a second set we studied the details of the distribution of CR energy in galaxy clusters re-simulated at high spatial resolution with AMR (Sect. 4.2).

4.1 Runs with fixed resolution

In a first set of cosmological runs we simulate the evolution of a box with a co-moving side of 80 Mpc, in a "concordance" cosmological Λ CDM model, with $\Omega_{\text{dm}} = 0.226$, $\Omega_b = 0.044$ and $\Omega_\Lambda = 0.73$. The normalization of the primordial index of density fluctuations was set to $\sigma_8 = 0.8$ and $h = 0.72$. The initial redshift of the simulations is $z_{\text{in}} = 30$. All runs are non-radiative, and neglect all non-thermal phenomena other than CR physics, such as energy release from stars and AGN or magnetic fields. When re-ionization in the early Universe is modelled, we follow the runtime recipe introduced in Vazza et al. (2010), where a simple prescription for a temperature floor in the simulation is adopted in the redshift range $7 \geq z \geq 2$ in order to mimic the re-ionization, as in Haardt & Madau (1996). Despite the moderate resolution achieved in these runs ($\Delta x \geq 122$ kpc/h), they allow us to test the role of

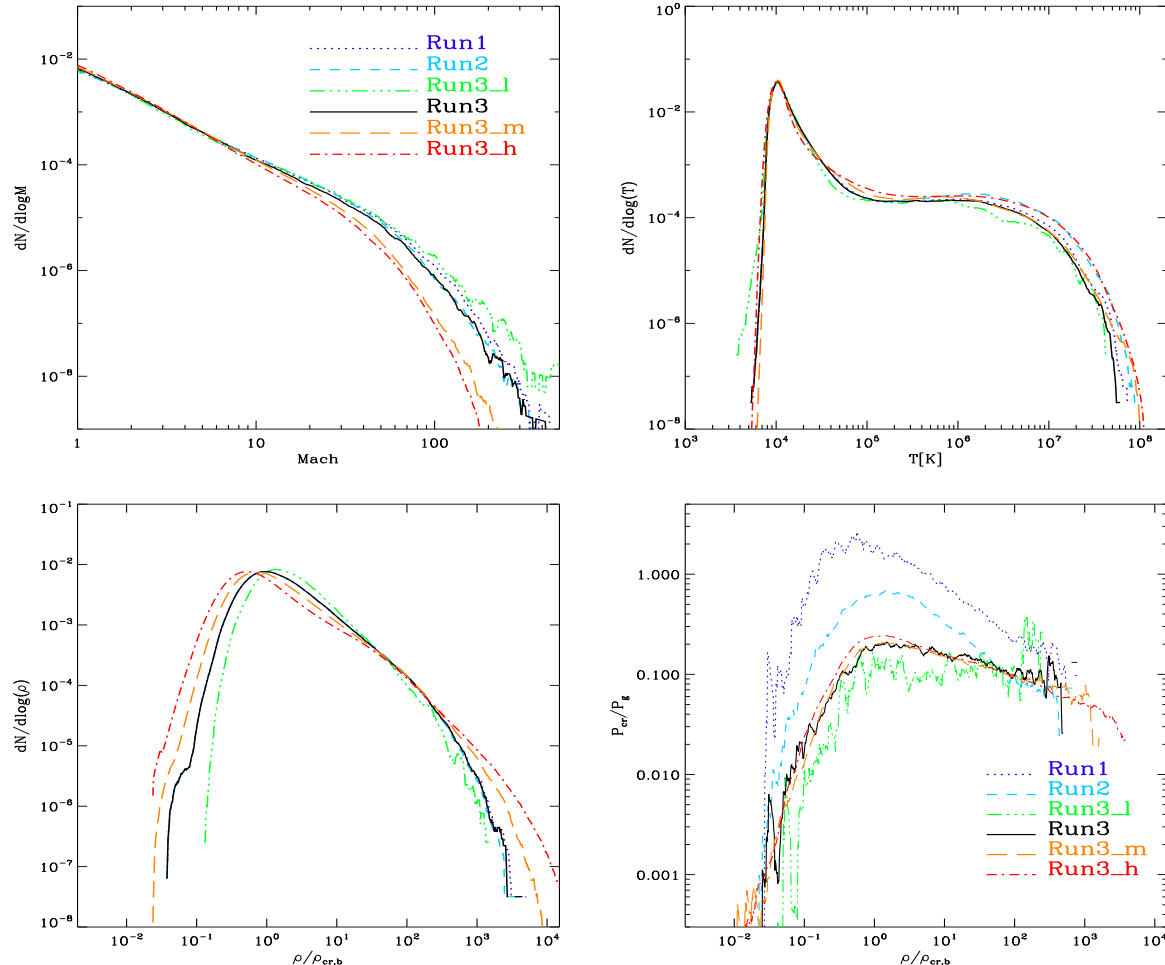


Figure 12. Comparison for the distributions of Mach number (upper left panel), gas temperature (upper right), gas density (lower left) and P_{cr}/P_g as a function of gas over-density (lower right) for runs Run1, Run2, Run3, Run3_L, Run3_m and Run3_h.

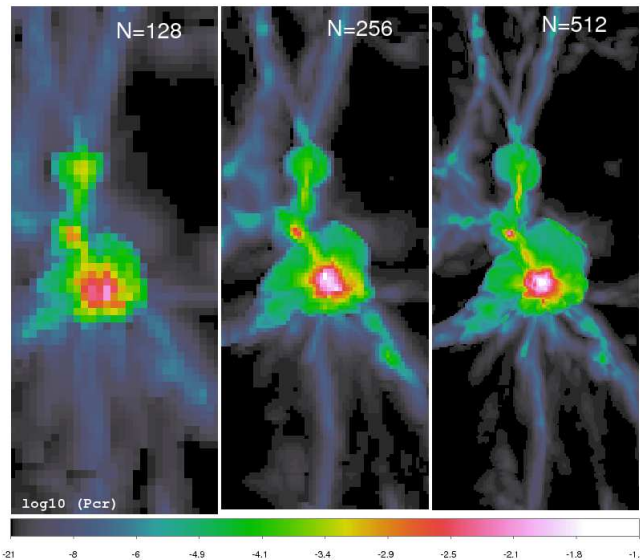


Figure 13. Maps of CR pressure as a function of resolution, for a slice of 20×60 Mpc and width 448 kpc/h, centred on the same massive galaxy cluster in the simulated volume (Run3, Run3_m and Run3_h are shown).

the parameters of our models. The summary of the 15 runs at fixed grid resolution is listed in Tab. 3.3.

Our fiducial model for simulating the evolution of CR energy in our ENZO cosmological runs is Run3 (and Run3_L, Run3_m and Run3_h at other resolutions, see below). In this model we adopt the full set of CR-modules of our implementation (injection at shocks, spatial advection, pressure feedback and the reduced thermalization). The injection of CRs at shocks starts from $z_{\text{cr}} = 6$, and for $\rho/\rho_{\text{cr},b} \geq 0.1$ (where $\rho_{\text{cr},b}$ is the critical baryon density of the Universe). The acceleration efficiency depends on M , as in Kang & Jones (2007).

In other runs we varied various parameters in order to study:

- the dynamical role of CRs in the evolution of large-scale structure with a simple non-radiative run (Run1). In this run, we inject and passively advect CRs in the simulated volume, but CRs do not couple to the baryonic gas (therefore they do not exert pressure nor do they cause reduced thermalization in the post-shock);
- the role of the reduced thermalization efficiency, by comparing Run3 with a run with CRs injection and pressure feedback but no reduced thermalization at shocks: Run2 (in this model the total energy at the shock is not conserved, since "new" pressure from accelerated CRs is just added to the system);
- the role of spatial resolution and DM mass resolution by re-

Table 1. Numerical and cosmological parameters for the runs employing fixed mesh resolution. The columns lists: ID of the run; mass resolution for DM; gas spatial resolution; number of grid cells. The last column reports mnemonics explaining the physical setups used in the run. "A"=advection of CR; "I"=injection of CR at shocks; "T"=reduced thermalization at the post-shock; "P"=pressure feedback of CRs. " $z_{\text{cr}} = 1, 29$ " mean that the injection in the runs was started at $z = 1$ and $z = 29$, respectively (or at $z = 6$ elsewhere). "no-re." means that the run does not model a re-ionization background (otherwise considered). " $\eta = 0.01$ " and " $\eta = 0.01$ " mean that the acceleration efficiency in the runs was kept fixed at these two values, independent on the measured Mach number (the $\eta(M)$ efficiency of Kang & Jones (2007) was used elsewhere). " M_{cr} " means that the Mach number used to compute $\eta(M)$ is the one from the total gas+CRs pressure jump, instead of the gas pressure jump only. " $\rho_{\text{cr}} = 10^{-3}, 10$ " means that we assumed minimum overdensity of 10^{-3} or 10 the background critical gas density to inject CRs ($\rho_{\text{cr}} = 0.1$ elsewhere).

ID	M_{dm} [M_{\odot}/h]	Δ_x [kpc/h]	N_{grid} [cells]	mnemonic
Run1	$5.1 \cdot 10^9$	448	128^3	AI
Run2	$5.1 \cdot 10^9$	448	128^3	AIP
Run3	$5.1 \cdot 10^9$	448	128^3	AIPT
Run3_l	$4.0 \cdot 10^{10}$	996	64^3	AIPT
Run3_m	$6.4 \cdot 10^8$	224	256^3	AIPT
Run1_h	$8 \cdot 10^7$	112	512^3	AI
Run3_h	$8 \cdot 10^7$	112	512^3	AIPT
Run3_no-re	$5.1 \cdot 10^9$	448	128^3	AIPT, no-re.
Run3_z1	$5.1 \cdot 10^9$	448	128^3	AIPT, $z_{\text{cr}} = 1$
Run3_z29	$5.1 \cdot 10^9$	448	128^3	AIPT, $z_{\text{cr}} = 29$
Run3_eta001	$5.1 \cdot 10^9$	448	128^3	AIPT, $\eta = 0.01$.
Run3_eta01	$5.1 \cdot 10^9$	448	128^3	AIPT, $\eta = 0.1$.
Run3_d0001	$5.1 \cdot 10^9$	448	128^3	AIPT, $\rho_{\text{cr}} = 10^{-3}$
Run3_d10	$5.1 \cdot 10^9$	448	128^3	AIPT, $\rho_{\text{cr}} = 10$
Run3_mcr	$5.1 \cdot 10^9$	448	128^3	AIPT, $M_{\text{cr}}, \eta = 0.1$

Table 2. Main characteristics of the simulated clusters. Column 1: identification number. Columns 2: total mass ($M_{\text{TOT}} = M_{\text{DM}} + M_{\text{gas}}$) inside the virial radius. Columns 3: virial radius, $R_v \approx 0.7 R_{200}$. Column 4: dynamical state at $z = 0$: MM=major merger cluster; ME=merging cluster, RE=relaxed cluster (see Sect.4.2 for further details).

ID	$M_{\text{TOT}} [10^{14} M_{\odot}]$	$R_v [\text{kpc}]$	dynamical state
E1	11.20	2670	MM
E7	6.52	2194	ME
E25	6.55	2369	MM
H1	3.10	1890	RE
H3	2.95	1710	ME
H5	2.41	1703	MM
H7	2.14	1410	RE

simulating Run3 with a coarser (Run3_l) and with two finer resolutions (Run3_m and Run3_h). For comparison, we also re-simulated the same setup of Run1 with 512^3 (Run1_h);

- the role of re-ionization by re-simulating Run3, for the extreme assumption of no re-ionization at all (Run3_no-re);
- the effect of assuming different epochs for the start of the injection of CRs at shocks, by investigating also the cases of $z_{\text{cr}} = 1$ (Run3_z1) and $z_{\text{cr}} = 29$ (Run3_z29);
- the effects of assuming a different minimum gas density for the injection of CRs at shocks, studying the case of $\rho/\rho_{\text{cr},b} = 10^{-3}$ (Run3_d0001) and $\rho/\rho_{\text{cr},b} = 10$ (Run3_d10);
- the effects of assuming fixed efficiencies for the acceleration of CR at all shocks: we investigated the "toy" models where the fixed efficiencies of $\eta = 0.1$ (Run3_eta01) and $\eta = 0.01$

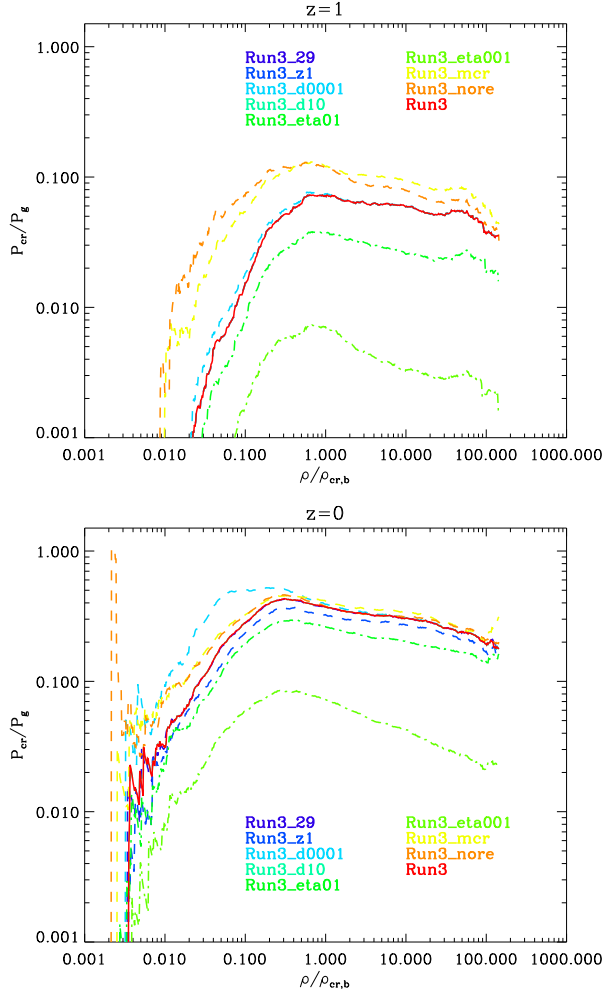


Figure 14. Average pressure ratio between CRs and thermal gas as function of the gas over-density in our runs at fixed grid resolution for $z = 1$ (top) and $z = 0$ (bottom).

(Run3_eta001) are adopted at all shocks (with no dependence on M);

- the differences caused by computing the Mach number based on the total pressure (Run3_mcr) instead of gas pressure, and applying the Kang & Jones (2007) efficiency.

4.1.1 Large-scale distributions of thermal gas and cosmic rays

We first test the CRI modules by comparing the large-scale distributions of Mach number, gas density, gas temperature and CRs pressure in Run1, Run2 and Run3 at $z=0.5$ (Fig.12). The presence of CRs has no strong dynamical effect in the evolution of thermal gas on these large scales. Some differences are found at large overdensities (where CR feedback reduces by a $\sim 5 - 10$ percent the largest over-densities in the box), and in the temperature distributions inside accretion shocks, $T > 10^5$ K. Inside large-scale structures, Run3 presents a small deficit of gas temperature compared to the standard simulation of Run1, due to the fact that part of the thermal energy at accretion shocks is channelled into energy of CRs. On the other hand, Run2 shows a significant excess of temperatures within the same regions compared to Run1. The obvious explanation for this is that the total energy at shocks is not conserved in

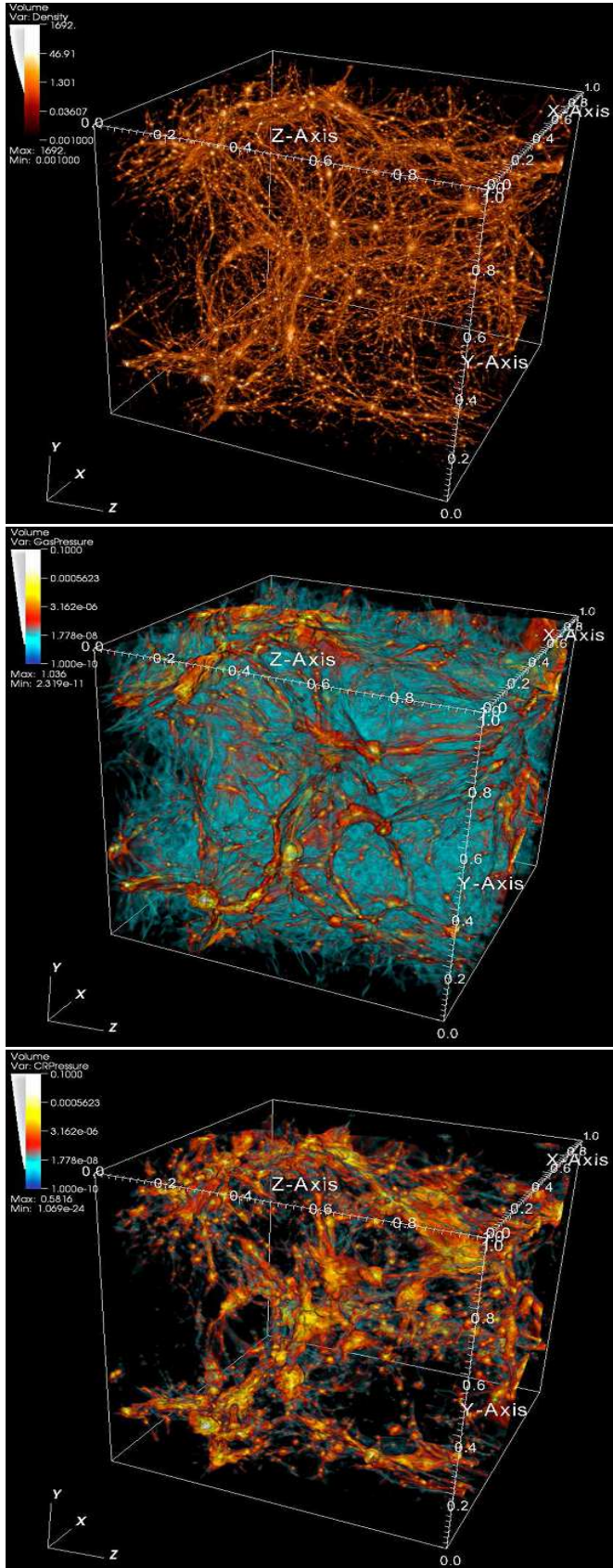


Figure 15. From top to bottom: 3-D volume rendering of gas density (in $[\rho/\rho_{\text{cr},b}]$), P_g and P_{cr} (arbitrary code units) for $(80\text{Mpc})^3$ in Run3_h at $z = 0$. Rendering performed with VISIT 2.3.1 (<https://wci.llnl.gov/codes/visit>).

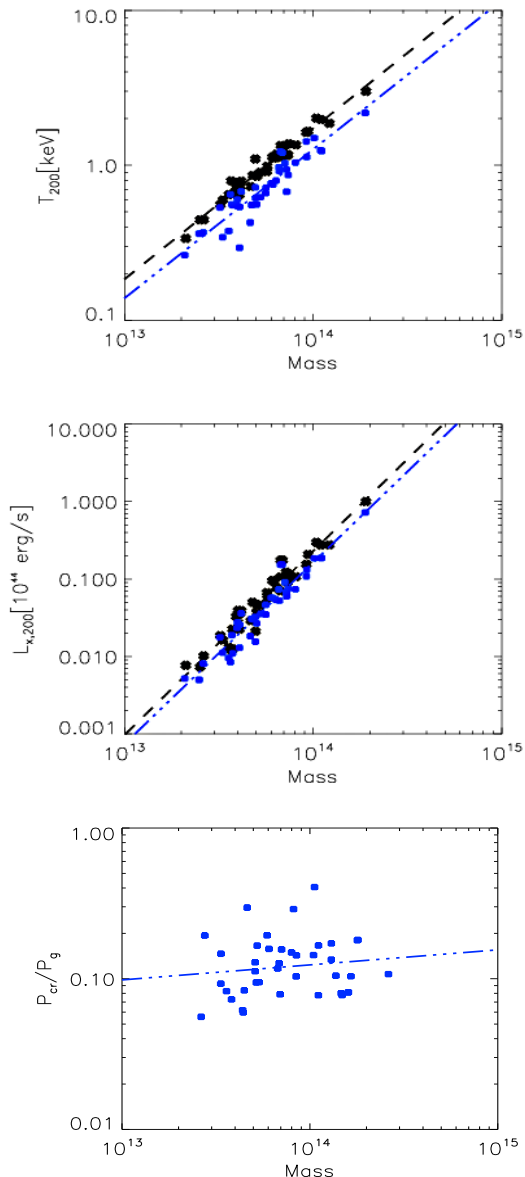


Figure 16. Scaling laws for the 40 most massive halos in Run1_h (black dots) and Run3_h (blue). Top panel: scaling between the total cluster mass, M_{200} (in M_\odot) and the mass-weighted temperature, T_{200} . Central panel: scaling between M_{200} and the total X-ray bolometric luminosity inside R_{200} , $L_{x,200}$. The straight lines show the best-fit for each sample. Bottom panel: average pressure ratio between CRs and gas for all clusters in Run3_h.

this run, but new energy is added to the system when new CRs are injected. This makes outer accretion shocks stronger over time in Run2, and therefore more efficient in thermalizing the medium.

An important proxy to understand the dynamical role of accelerated CRs is the pressure ratio between CRs and thermal gas, P_{cr}/P_g , as a function of cosmic over-density (last panel of Fig.12). The trend of this ratio is broadly similar in all runs, with a maximum at the over-densities close to the critical one. In our fiducial model (Run3) this maximum is $P_{\text{cr}}/P_g \sim 0.2$, and smoothly declines to $P_{\text{cr}}/P_g \sim 0.04 - 0.08$ for $\rho/\rho_{\text{cr},b} \approx 100$. This ratio is larger if the reduced thermalization at shocks is not included

$(P_{\text{cr}}/P_g \sim 0.5$ at the maximum in Run2) and even larger if the accelerated CRs are just passively advected in the simulation (Run1).

We test the effect of spatial resolution and DM mass resolution by re-simulating the same setup of Run3 with a smaller (Run3_l, using 64^3 cells and $m_{\text{dm}} = 4.0 \cdot 10^{10} M_\odot/h$) and at two larger resolutions (Run3_m with 256^3 and $m_{\text{dm}} = 5.1 \cdot 10^9 M_\odot/h$, and Run3_h with 512^3 and $m_{\text{dm}} = 8 \cdot 10^7 M_\odot/h$). The final maps of CR pressure for the most massive galaxy cluster in the box is shown in Fig.13, and suggests that the CR pressure at the largest scales in the simulation are very similarly reconstructed at all resolutions. The increase in resolution, however, produces a more sub-structured distribution of CR pressure inside clusters. As expected from previous studies (Ryu et al. 2003; Vazza et al. 2009, 2011b), the increase in the spatial resolution leads to a sharper reconstruction of shock waves, and to a lowering of the Mach number of strong accretion shocks. When averaged over the whole cosmological volume, very good convergence in the volume distribution of simulated large-scale shocks is achieved at the resolution of $\Delta x \sim 200$ kpc/h, corresponding to the resolution achieved in Run3 (Fig.12). The average pressure ratio P_{cr}/P_g shows a very regular behaviour across resolutions, and a nearly converged trend with over-density for $\rho/\rho_{\text{cr,b}} > 1 - 10$. At the maximum resolution here ($\Delta x = 112$ kpc/h) the average pressure ratio at the scale of the innermost cluster regions is $P_{\text{cr}}/P_g \sim 0.05$. In Sec.4.2 we will show that this trend is confirmed even at larger resolution, using adaptive mesh refinement for a subset of massive galaxy clusters.

We finally tested the various assumptions related to the injection of CRs by modifying the setup of Run3. For instance, a suitable minimum magnetic field is required for DSA to work, and therefore it is reasonable that the acceleration of CRs takes place only at over-densities large enough to have had the opportunity to generate sufficiently high magnetic fields. Assuming a minimum over-density for the injection of CRs in the simulation also reduces the number of un-necessary computations.

Figure 14 summarizes the differences in the final distribution of P_{cr}/P_g as a function of gas over-density in the simulated volume, for all runs with varied parameters of CR acceleration but identical spatial and DM mass resolution, at $z = 1$ and $z = 0$.

The differences are somewhat larger at $z = 1$ (top panel) and become less significant for large-scale structures at $z = 0$ (bottom). At all epochs, the maximum of the pressure ratios is always found at $\rho \sim \rho_{\text{cr,b}}$, meaning that the accretion regions of large-scale structures are the locations where CRs can have the largest dynamical role. As seen above, the pressure ratio inside large-scale structures is usually much smaller, $P_{\text{cr}}/P_g \sim 0.1$ for $\rho/\rho_{\text{cr,b}} \geq 10^2$, in all tested models.

When the acceleration efficiency depends on the Mach number, we find that the pressure ratio for all over-densities $\rho/\rho_{\text{cr,b}} \geq 1$ is almost independent of the assumptions (on the initial epoch, minimum over-density for injection, re-ionization, etc.). Differences of one order of magnitude in the pressure ratio between the different re-simulations can be found only for densities below the critical one. There the effects of re-ionization and of the assumed first epoch of DSA are still present at $z = 0$.

In the runs using a fixed acceleration efficiency the two trends for $\rho/\rho_{\text{cr,b}} > 1$ are rescaled version of the same profile. In particular the model with the fixed efficiency of $\eta = 0.1$ lies just below our fiducial model with the efficiency of Kang & Jones (2007) for

$\eta(M)$. This suggests that at $z = 0$ the bulk of the injection of energy in CRs happens with an average Mach number of $M \sim 2 - 3$ (typical of internal merger shocks), which are characterized by an acceleration efficiency of $\eta \sim 0.1 - 0.2$ (see also Fig.4). This is also in line with our previous estimates based on post-processing the time evolution of the energy processes at cosmological shocks in ENZO runs (Vazza et al. 2009).

Given the present large theoretical uncertainties conditions of DSA in the early universe, and in presence of small gas density and very weak magnetic fields, it is reassuring that such uncertainties contribute only modestly to the final distribution of CR energy inside all structures, for $z < 1$. In essence, we can assume that the average distribution of CR energy inside large-scale structures is almost totally dominated by the dynamics of accretion shocks and merger shocks in the hot and dense baryon plasma, within the last ~ 8 Gyr.

This ensures that, at least to first approximation and limited to regions of radii $\sim 2 - 3 R_{\text{vir}}$ around galaxy clusters, the statistics provided by our method for CRs is very robust, once an acceleration scenario for CRs is specified.

4.1.2 Scaling relations for clusters

We first studied the global effects of CR dynamical feedback on a statistical sample of galaxy clusters, extracted from the two most resolved runs at fixed resolution (Run1_h and Run3_h).

The spatial resolution of 112 kpc/h (which also represents the softening for the computation of the gravitational force) is suitable to study the outer accretion regions of galaxy clusters and groups, but not to resolve in detail the mixing in the innermost cluster regions, and the evolution of cluster cores. For this reason, we consider the sample of clusters useful to study the effect of CR dynamics in the region inside R_{200} (where R_{200} is the radius enclosing an average density of 200 times the cosmic critical density). Clusters were extracted with a halo finder based on spherical over-density (as in Gheller et al. 1998). A more detailed study of the distributions of CRs inside clusters, at a higher resolution, is presented in Sec.4.2.

Our volume of $(80\text{Mpc})^3$ contains ~ 50 halos with a total mass larger than $10^{13} M_\odot$ at $z = 0$ (8 with $M > 10^{14} M_\odot$). The panels in Figure 15 give the visual impression of the number of halos in the simulated volume, and the large-scale distributions of gas and CR pressure associated with them. Since the injection of CRs occurs only for a large enough overdensity ($\rho \geq 0.1\rho_{\text{cr,b}}$), the 3-D distribution of CR pressure has a much lower volume filling factor than that of gas pressure.

The comparison of the T_{200} vs M_{200} relation and of $L_{X,200}$ vs M_{200} (i.e. average temperature, total mass and bolometric X-ray luminosity inside R_{200}) for the most massive clusters of both runs is shown in the top panels of Fig.16.

Given the limitations of physical processes included in our runs (no radiative cooling, star formation and feedback from supernovae and AGN), the comparison of these two runs is helpful to highlight the effects of simulated CRs in clusters, while they do not have a strong prediction power on observed scaling relations.

In the two runs the self-similarity of cluster relations is preserved, but the dynamical feedback of CR energy injected at shocks modifies the normalization of both scaling by ~ 20 percent for (M_{200}, T_{200}) and for $(M_{200}, L_{X,200})$. As will be shown in the following (Sec.4.2) this is a result of a slightly modified distribution of gas matter density inside halos. The last panel of Fig.16 shows

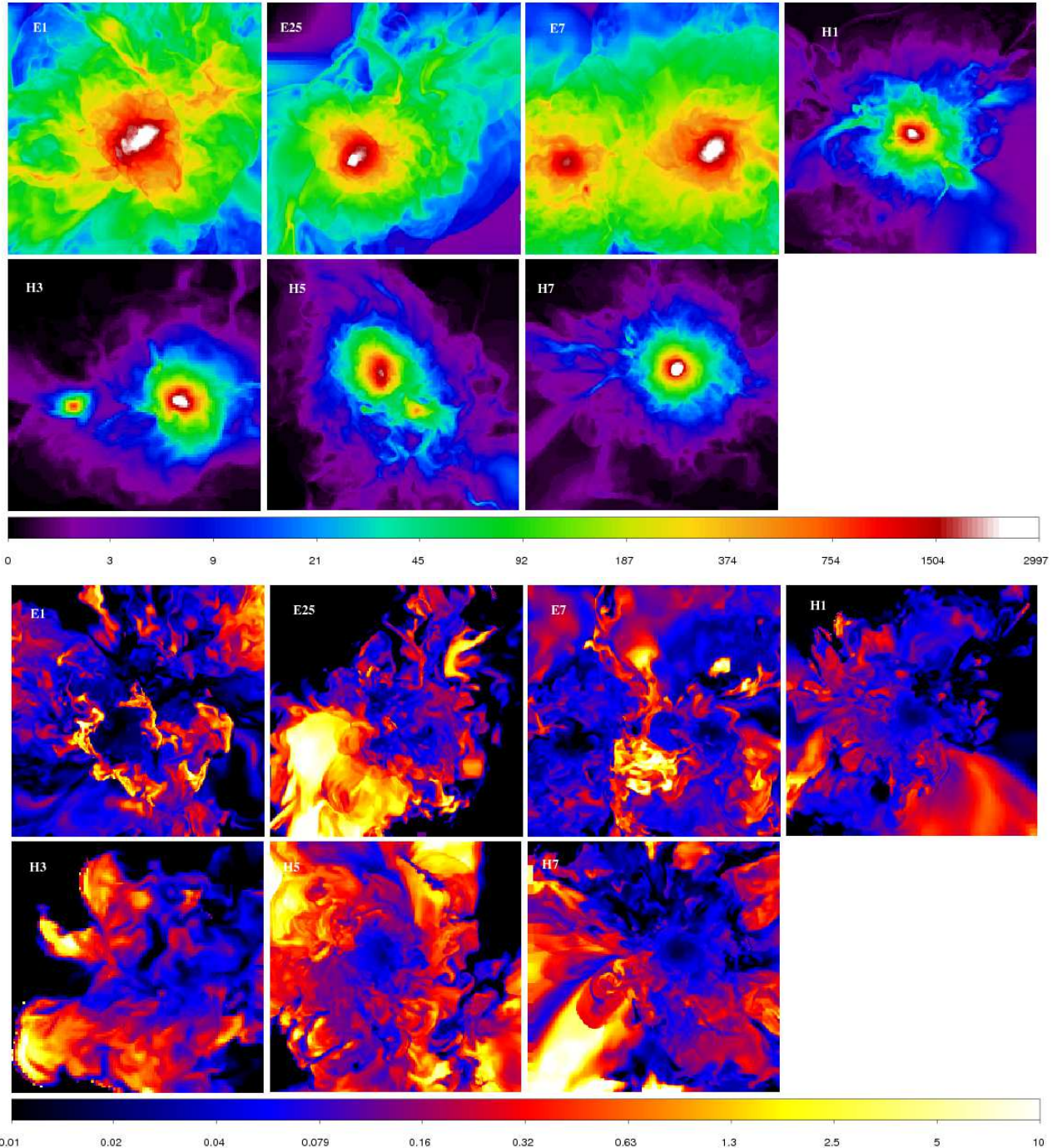


Figure 17. Top panels: maps of gas density for slices of depth 25 kpc/h through the centre of re-simulated clusters of various masses at $z = 0$ (color panel in $\rho/\rho_{\text{cr},b}$). Bottom panels: maps of CRs to gas pressure ratio for the same regions. Each panel has a side of ≈ 10 Mpc.

the pressure ratio between CRs and gas within R_{200} for all objects of Run3_h. The majority of clusters has a ratio of the order of $P_{\text{cr}}/P_{\text{g}} \sim 0.1$, with an almost constant average ratio across one order of magnitude in mass (even though the distribution has a quite large scatter, and no simple trend with total mass can be detected).

4.2 Adaptive mesh refinement runs

A second set of cosmological simulations was produced with adaptive mesh refinement, achieving almost uniform high spatial resolution within cubic boxes of side length $\sim 4 - 6R_{200}$ for several galaxy clusters in the mass range of $2 \cdot 10^{14} \leq M/M_{\odot}/h \leq 2 \cdot 10^{15}$. These runs are computationally fairly expensive (e.g. $\sim 2 \cdot 10^4$ hours of CPU time for the most massive clusters), and in this work we limit ourselves to the analysis of 7 re-simulated objects, selected from catalogues of clusters already presented in

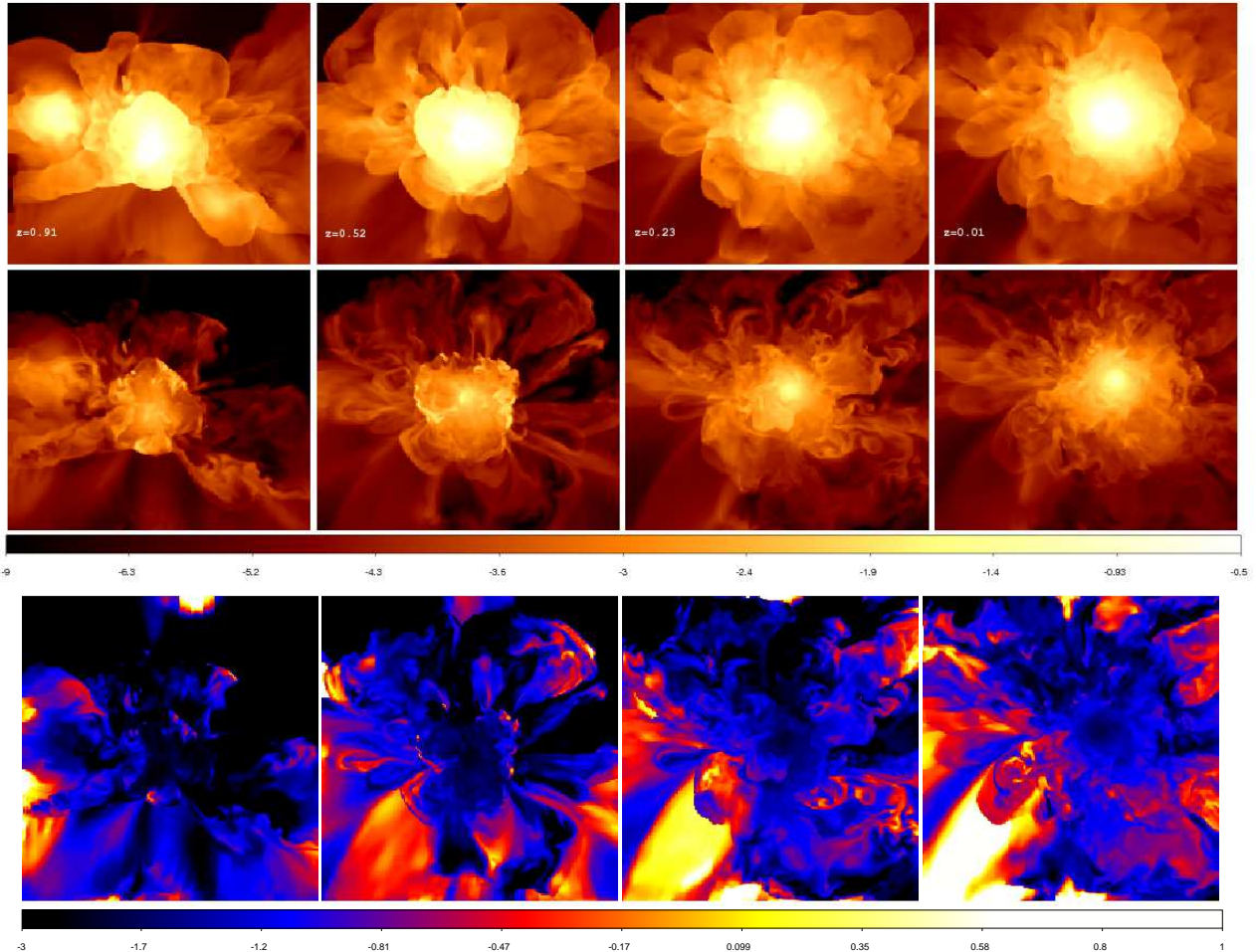


Figure 18. Maps of gas pressure (first row, shown is $\log_{10}(P_g)$), CR pressure (central row, shown is $\log_{10}(P_{\text{cr}})$) and ratio of the two (last row, $\log_{10}(P_{\text{cr}}/P_g)$) for the major merger cluster H7 at four epochs. Each slice has depth 25 kpc/h and side 10 Mpc/h.

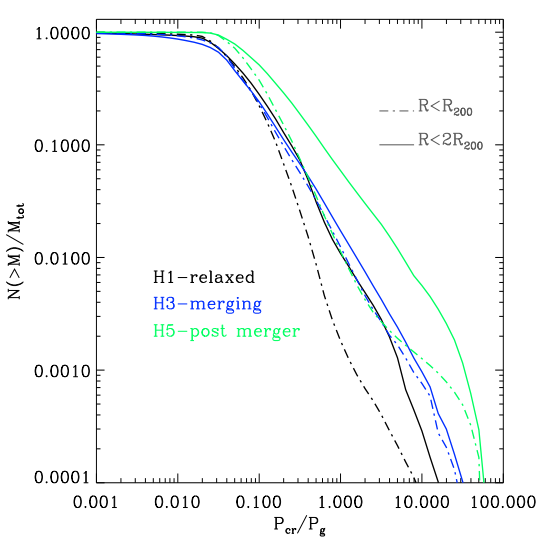


Figure 20. Cumulative gas mass distribution as a function of P_{cr}/P_g , for clusters H1, H3 and H5 at $z=0$. The solid lines are for the volume inside $\leq 2R_{200}$, the dot-dashed lines are for $\leq R_{200}$.

Vazza et al. (2010) and Vazza et al. (2010), in order to sample different masses and dynamical state of the ICM.

The use of AMR is necessary here to model the turbulent motions in mergers, which may affect the properties of transport of CR energy within clusters over time. In addition, the increased resolution in capturing shocks can enhance our modelling of CR injection at internal shocks.

All objects have been re-simulated at high spatial and DM mass resolution starting from parent simulations at lower resolution, using nested initial conditions (e.g. Abel et al. 1998). The mass resolution for DM inside the high resolution region where the clusters form is $m_{\text{dm}} = 6.7 \cdot 10^7 M_{\odot}$, the coarsest spatial resolution inside this region is 200 kpc/h while the peak one is 25 kpc/h. In general a fraction of $\sim 60 - 80$ percent of the total volume inside $\leq 2R_{200}$ is simulated at the highest available resolution by the end of the simulation (Vazza et al. 2010). In these runs we triggered mesh refinement by standard gas/DM over-density criteria (e.g. O’Shea et al. 2004) and velocity jumps (as in Vazza et al. 2009).

Table 2 summarizes the main properties of each object. The last column indicates the dynamical state of the cluster. Following Vazza et al. (2010) we estimated the dynamical state of each cluster at $z=0$ from its total matter accretion history for $z < 1.0$ (in the case of the lowest masses systems, $< 3 \cdot 10^{14} M_{\odot}$, we consider instead

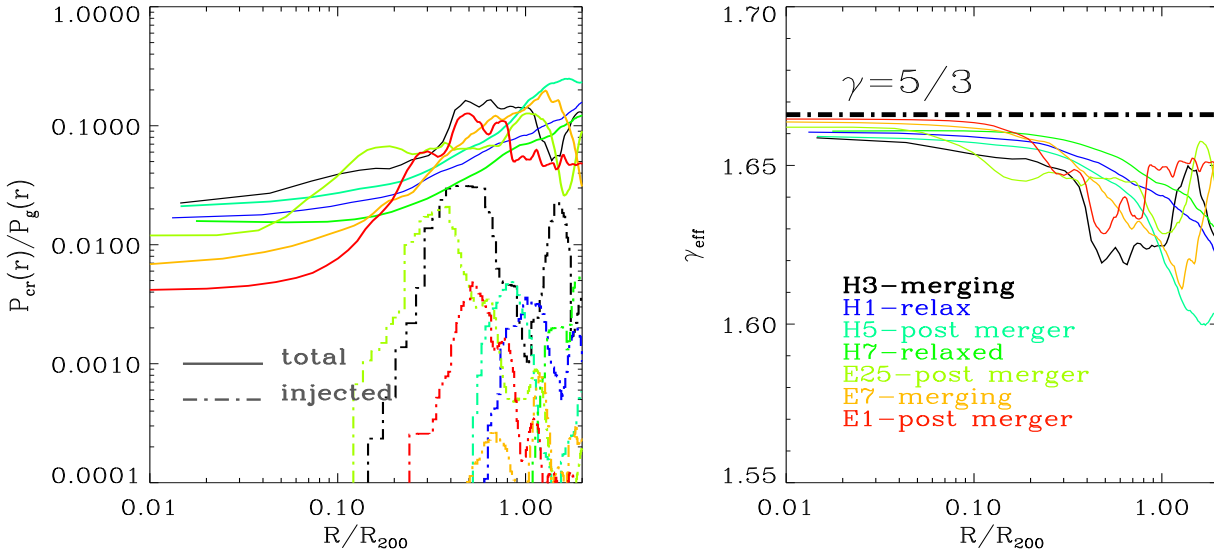


Figure 19. Left panel: radial profiles of average CRs to gas pressure ratio for the sample of re-simulated clusters with AMR at $z = 0$ (solid lines), and pressure ratio only for the CRs injected during the last $\Delta t \sim 0.1$ Gyr (long dashed lines). Right panel: average effective (pressure weighted) adiabatic index for the same clusters at $z = 0$.

$z < 0.6$ for the same analysis, given their shorter dynamical times). If a system experienced an increase of total matter by 30 percent of more within 1 Gyr of time, we classify it as a "post merger" systems, or "relaxed" otherwise. In the case of systems without a major merger in the past, but having an ongoing merger process (estimated from the ratio between total kinetic and thermal energy within R_{200}) the system is classified as "merging".

Figure 17 shows cuts through the centre of mass of each object of the sample, reporting the gas density (left panels) and the pressure ratio within each cell of the 25 kpc/h slice (right). Substantial morphological differences are present, related to the dynamical state of the cluster: in merging systems (e.g. E7, H3) the presence of close companions and ongoing large-scale accretions drive streams of enriched CRs gas in the ICM, even close to the main cluster centre. In post-merger systems (e.g. E1, H5) the regions of large $P_{\text{cr}}/P_{\text{g}}$ ratio are well associated with merger shock waves, which expand out of the innermost cluster regions.

The long time evolution for one of these systems (H7) is shown in Figure 18 for the epochs of $z = 0.91$, $z = 0.52$, $z = 0.23$ and $z = 0.01$. Two powerful merger shocks are launched just after the collision of the cluster cores at $z = 0.91$, and become powerful sites for the injection of new CRs in the ICM. While these shocks expand into the outer cluster regions, their Mach number increases. Just downstream of the shocks, the local pressure ratio becomes of the order of $P_{\text{cr}}/P_{\text{g}} \sim 0.3$, while inside the hot core region of the merger remnant the pressure ratio is small, $P_{\text{cr}}/P_{\text{g}} \sim 0.02 - 0.05$. This happens because internal merger shocks in their initial phase are weak, $M \sim 2$, and thus more efficient in heating the ICM than in injecting new CRs. On the other hand while they expand their Mach number increases due the drop in temperature of the ICM, and the efficiency of injection of CRs is larger. At later times, the cluster is characterized by a pretty regular density structure for $< R_{200}$, and regions of $P_{\text{cr}}/P_{\text{g}} > 0.1$ can be found only near the outer accretion regions, and also along filaments of cold gas ($T \sim 10^5$ K) in some sectors of the cluster.

4.2.1 Radial profiles of CRs

Despite the different dynamical states present in our cluster sample, the radial profiles of the pressure ratio within each system at $z = 0$ are rather similar (left panel of Fig.19)¹. They show a behaviour similar to that of thermal pressure, and are slightly flatter approaching $\sim R_{200}$. Within the core region of our systems, the pressure of CRs is $\sim 0.02 - 0.04 P_{\text{g}}$, and it increases to $\sim 0.1 P_{\text{g}}$ approaching $1 - 2 R_{200}$. In the same panel, we also show the pressure ratio of the CRs injected at shock waves during the last time step of each run ($\Delta t \sim 0.1$ Gyr). Only in the case of the merging system H3, a large amount of freshly injected CR pressure at a peripheral shock is comparable with the thermal pressure, while otherwise the pressure injected at shocks at late time is on average just a small fraction of the gas and CR pressure. The right panel of Fig.19 shows the radial profile of the pressure-weighted average effective adiabatic index, γ_{eff} . Given the small ratio of CR to gas pressure in the innermost regions of clusters, γ_{eff} is very close to the non-relativistic value of $5/3$ until the outer accretion regions are reached. These trends are quite similar to what is reported in Pfrommer et al. (2007) for non-radiative simulations with GADGET2. However, we notice that our profiles of CR pressure are significantly flatter, and our runs tend to concentrate less CRs in the innermost cluster regions (e.g. Pfrommer et al. 2007; Pinzke & Pfrommer 2010). In Sec.5 we will discuss the possible reasons for this.

To highlight any dependence on the dynamical state of clusters we will focus in the following on three representative objects in the sample: H1 (relaxed), H3 (merging) and H5 (post-merger). These three clusters have a similar final total mass but very different dynamical histories.

For each of them we computed the cumulative gas mass distribution as a function of P/P_{g} (Fig.20). In all cases, roughly ~ 90

¹ We note that characterizing the exact centre of the most perturbed systems is not trivial, see also Vazza et al. (2011a) for a similar discussion in the case of radial profiles of turbulent energy.

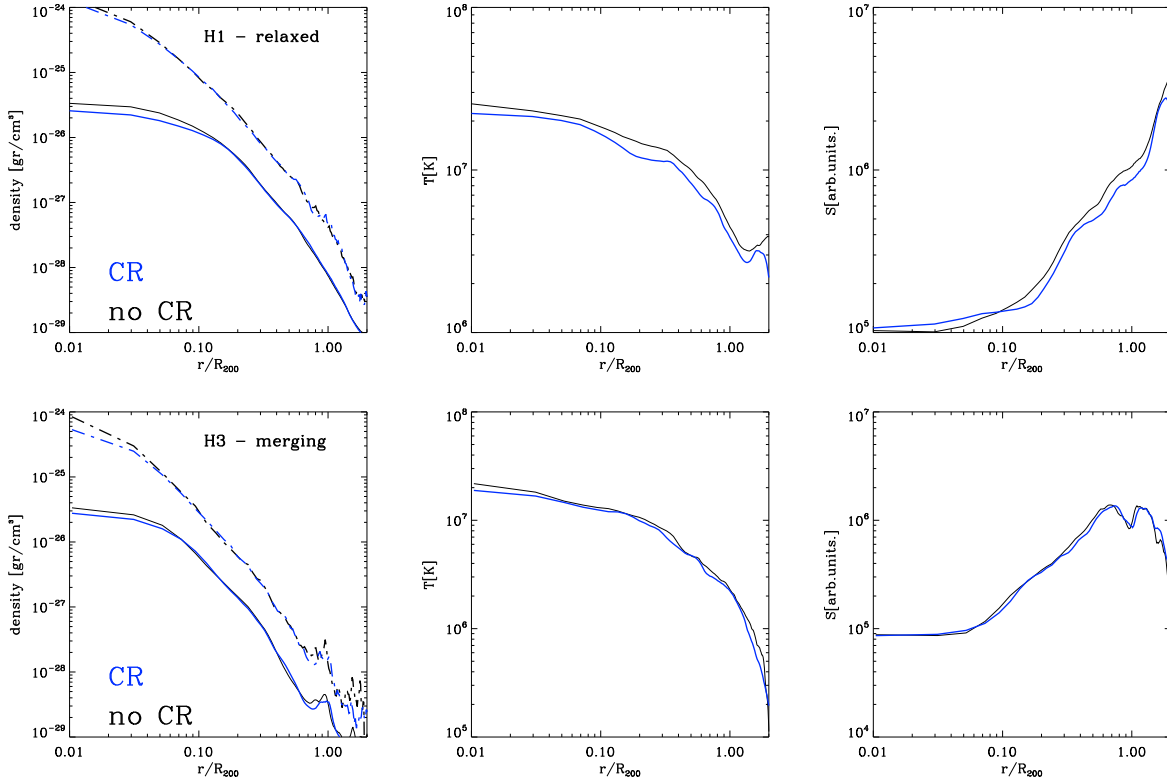


Figure 21. Comparison of radial profiles of gas and DM density (left column), gas temperature (middle) and entropy (right) for re-simulations of cluster H1 and H3 with and without CR physics.

percent of the gas mass inside R_{200} is characterized by a small pressure in CRs, $P_{\text{cr}}/P_g \leq 0.1$. The post-merger system H5 is characterized by the largest gas mass with greater CRs pressure, followed by the merging system H3. The differences between the dynamical states become more prominent by considering the distributions inside $< 2R_{200}$, highlighting the role of large-scale patterns of accretion even for clusters with quite similar final mass.

It is interesting to compare the runs with injection and feedback from CRs to the standard non-radiative re-simulations of the same systems. Some very general trends emerge by computing the 3-D radial profiles of gas density, gas temperature and gas entropy (Fig. 21): the innermost gas density is lower by a few percent in runs with CR physics. The gas entropy is correspondingly higher, while the gas temperature is slightly lower at all radii. Also the DM density in the innermost radial bin is decreased by a similar amount. As shown also with fixed grid simulation (Sect. 4.1.2) this is a very general outcome of our runs, and very similar results are also found for all the other re-simulated clusters of our sample.

The reason for this small difference with standard runs is non-trivial. Starting from the early formation of cosmic structures, the injection of CRs is efficient in the outer accretion regions, gradually leading to a drop of the effective adiabatic index in these regions. This enhances the gas density in the outer regions, and leaves slightly less gas matter available for the inflow towards the central regions of clusters. While expanding into the rarefying cosmic environment outside of structures, the relative pressure ratio of CRs is further increased because of their softer equation of state (in addition, the outer thermal pressure is decreased by our modelling of the reduced thermalization efficiency at the post-shock). This pro-

cess leads overall to an enhanced total (gas+CR) pressure of the outer accretion regions of forming structures, compared to standard runs without feedback from CRs. At the same physical time, the structures simulated with CR feedback have a more extended and dense envelope of accretion regions. This effect is similar to what was already found for the Zeldovich collapse test (Sect. 3.3). In fully cosmological simulations this effect is amplified by the fact that the expansion in 3-D of the outer cluster shells makes the relative increase of CR pressure more significant. We further explored the reasons of the above differences between simulations with and without CR feedback in the Appendix A.

4.2.2 Properties of X-ray emission and SZ signal

Differences in the 3-D distribution of thermal gas between runs with and without CRs lead also to significant differences in X-ray emission and SZ effect (e.g. Pfrommer et al. 2007). We investigate here the projected emission maps of the simple bolometric X-ray luminosity ($L_X \propto \int n_e^2 T_e^{1/2} dV$, where n_e is the thermal electron density and T_e is the thermal electron temperature, which we assume equal to the gas temperature for simplicity) and of the integrated thermal Sunyaev-Zeldovich effect ($Y \propto \int n_e T_e dV$) along different projections of our clusters.

In Fig. 22 we show the 3 maps of Y for the merging cluster H3 at $z=0$ (simulated without CR feedback, top, and with CR feedback, central panel), and the pixel by pixel ratio obtained by dividing the maps on the top panels with the corresponding ones from a re-simulations of H3 without CR feedback (bottom panels).

The large-scale morphology of the SZ effect in the two cases

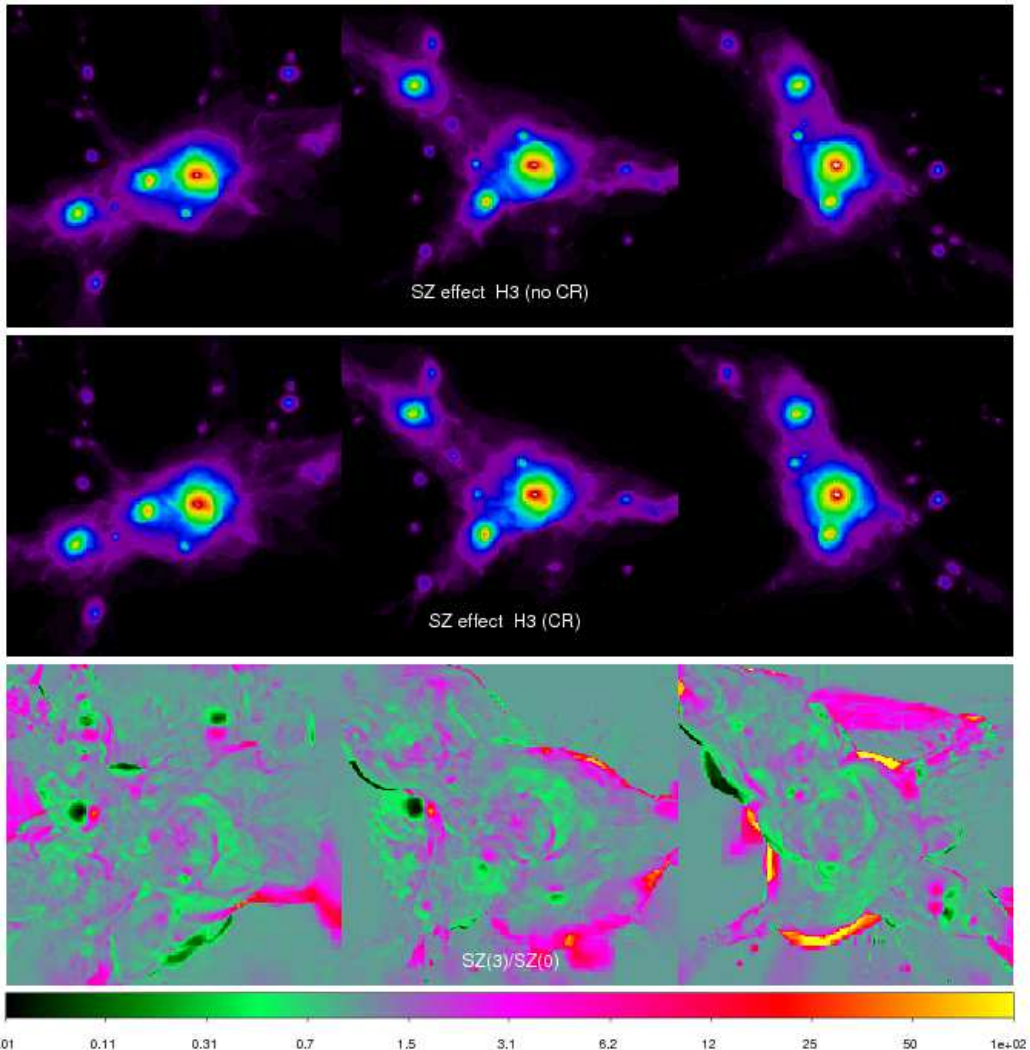


Figure 22. Top panels: projected Y parameter for the merging cluster H3 at $z=0$ in the run with CR physics, along three projection axes. Bottom panels (and color bar): pixel by pixel ratio between the simulated maps of SZ effect for the same cluster, obtained with (blue) and without (black) our implementation of CR physics.

is extremely similar, with minor differences at small scales that can be partially explained by the different time-stepping of the two runs (which affect the exact 3-D position of accreted gas clumps in the main cluster atmosphere). The most prominent difference is related to the outer accretion shocks, at $\sim 1 - 2R_{200}$, where the run with CR feedback produces a stronger SZ signal. The bulk of this effect is mostly related to the physical position of the envelope of outer accretion shocks in the run with CRs, which is farther from the cluster centre of $\sim 50 - 100$ kpc/h. Again, this is similar to what observed in the Zeldovich collapse test (Sect.3.3): the physical effect of a mixture of CRs and thermal gas in the outer regions produces and overall slightly accelerated expansion of the outer shell at the same time step. To show that this trend is general to all resimulated clusters, we show in Fig.23 the ratio of the radial profiles of projected maps in clusters H1, H3 and H5, considering both X-ray emission (solid lines) and SZ signal (dashed). In order to limit the very localized effect of gas clumps with small differences in position we post-processed our simulated maps using a filtering technique similar to Roncarelli et al. (2006), already applied to our clusters in Vazza et al. (2011c). With this technique, the 1 percent

X-ray brightest pixels at each radial bin are excised from the raw maps, and replaced with the average value at the same radius, thus highlighting the large-scale behaviour of the smooth gas component only.

All clusters present a similar deficit of L_X and Y for $r < 0.5R_{200}$, of the order of $\sim 10 - 30$ percent in the case of X-ray emission and of $\sim 5 - 10$ percent in thermal SZ. In the accretion regions close to $\sim R_{200}$, clusters simulated with CR feedback tend to have enhanced L_X emission and Y , thus producing slightly flatter profiles compared to the runs without CRs. However, a precise quantitative estimate is more difficult, due to the systematically larger radius of accretion shocks. Taking the most relaxed cluster of our sample (H1) as a reference, we find that L_X and SZ effect increase at least by $\sim 20 - 30$ percent. In the case of merging clusters the maximal difference can be as large as a factor $\sim 3 - 4$ in some projections.

Combined with the findings of the scaling for (T_{200}, M_{200}) and $(L_{X,200}, M_{200})$ for the sample of clusters simulated with fixed mesh resolution (Sect.4.1.2), these results suggest that the injection

and pressure feedback of CRs in large-scale structures can be responsible for small but measurable effects. Even if the inclusion of additional physical processes in our runs can somewhat alter the small-scale distribution of CRs in the innermost cluster regions (given that cooling, star formation, AGN and magnetic field should be most important for $\sim 0.1R_{200}$), our findings for the large scales are more robust against the inclusion of these processes, given that heating from shock waves is expected to be the most physically relevant process at $\sim R_{200}$. Interestingly, a recent analysis of a large set of clusters observed with *ROSAT* out to $\sim R_{200}$ presents the evidence for slightly flatter outer profiles of gas density and L_X , compared to the expectations of simple non-radiative simulated cluster runs (Eckert et al. 2011b). Even if several explanation are possible for this, such as gas clumping, the departure from simple non-radiative profiles is of the same order as that caused by the presence of CRs.

Hence, the effect of CRs may thus have intriguing consequences in the physical interpretation of recent observation of galaxy clusters close to $\sim R_{200}$ (e.g. Bautz et al. 2009; George et al. 2009; Simionescu et al. 2011; Urban et al. 2011; Eckert et al. 2011a), as well as in the use of cluster scaling relations to perform "high-precision" cosmological studies (e.g. Hallman et al. 2006; Pierre et al. 2011, and references therein).

The application of cosmological simulations including feedback from CRs were performed in the recent past with a modified version of the SPH code *GADGET2* (Springel 2005; Pfrommer et al. 2007; Jubelgas et al. 2008). Contrary to our results, these works found that the inclusion of CRs leads to an increase of the central gas density (and thus the X-ray luminosity and the amplitude of the SZ effect) inside $\sim 0.1R_{200}$, while leaving the outer cluster regions essentially un-modified. This is puzzling since the radial profile of effective adiabatic index in non-radiative runs of Pfrommer et al. (2007) is very similar to ours (Sect.4.2.1).

Understanding the reason of this difference is not trivial, given the different numerical techniques and physical assumptions. We argue that most of the differences in the two schemes are due to the different way in which the injection of CRs and their transport take place. In a recent comparison of cosmological runs with *GADGET* and ENZO (Vazza et al. 2011b), we investigated in detail how matter from accreted gas satellites is shock-heated and distributed within the main cluster volume. The result is that while in *GADGET* matter from satellites usually retains its internal low entropy gas, delivering it to main cluster centre ($R < 0.1R_{200}$), in ENZO the gas matter from satellites is efficiently shock heated and deposited at much larger radii, $> 0.5R_{200}$ (see also Vazza 2011, for similar results with AMR runs). Very similar conclusions have been recently presented by Simionescu et al. (2011), who compared the results on accreted cluster satellites in *GADGET* and in *AREPO*. In the same work, we also showed that while the total energy flux of shock waves in the cosmological volume is quite similar in the two codes, the average properties of external accretion shocks are not: shocks are sharper, more regular in shape and stronger in grid codes. This produces a larger entropy generation in accreted clumps in grid simulations, while much more pre-shock entropy generation is measured in SPH runs. The effect is much more significant than the differences due to simple resolution effects at $\sim R_{200}$ in the two approaches. Therefore, also the accretion of shock-injected CRs from accreted gas clumps would look quite different in the two methods, once the injection of CRs is followed in run-time. While in *GADGET* runs we expect that CRs from clumpy accretion is delivered in the centre of galaxy clusters, in a grid code such as

ENZO the injection of CRs (and their dynamical feedback) mostly takes place at large cluster radii. The net effect is that while in SPH the modification of CRs feedback causes a larger compressibility in the centre of structures (and hence an increase of gas density to keep pressure equilibrium), in grid codes the modification of CRs dominates at large radii, enhancing the compressibility of the outer cluster layers already since the early times of structure formation (see Sect.3.3 and Appendix). Based on our results in Vazza (2011) and Vazza et al. (2011b), and following previous results from other groups (e.g. Agertz et al. 2007; Wadsley et al. 2008; Mitchell et al. 2009), the most likely explanation for the above differences is the role of artificial viscosity in the standard SPH formulation, and the existence of sizable pre-shock entropy generation in the standard SPH runs (O'Shea et al. 2004). Incidentally we notice also that a trend for gas density, X-ray luminosity and gas temperature very similar to ours has been reported by Ryu & Kang (2004) for grid simulations with pressure feedback, where CRs were injected in the cluster volume by AGN-like sources.

5 DISCUSSION

Our simulations with an implementation of CR physics in ENZO allow us to highlight the role of CRs injected at cosmological shocks. Because of the numerical and physical complexity of CRs injection and CR feedback on the ICM plasma, a few strong assumptions had to be made.

First, the acceleration efficiency at shocks is presently uncertain. We adopted the efficiency of Kang & Jones (2007), which is based on studies of particles acceleration in SN remnants (however in Sec.4.1 we tested also fixed efficiencies). The details of particle acceleration in the regime of Mach numbers typical of the ICM, $M \leq 5 - 10$ are not yet robustly constrained by the theory, due to the difficulty of modelling the large spatial and temporal scales involved in the diffusive acceleration at such shocks (e.g. Kang & Ryu 2010). More recently, interesting studies employing particle-in-cells methods investigated additional acceleration mechanism for particles at shocks (e.g. shock drift acceleration), suggesting the possibilities of a different trend with Mach number (Gargaté & Spitkovsky 2011). Our treatment of CRs injection in ENZO runs will enable us to perform cosmological simulations with any given prescription for the functional dependence between acceleration efficiency and background properties of the ICM. However, the injection of CRs in the early Universe ($z \gg 2$), and in the most rarefied cosmic environment ($\rho/\rho_{cr,b} \ll 1$) is uncertain because the evolution of magnetic fields outside large-scale structures is still subject to debate (e.g. Zweibel & Heitsch 2008; Miniati & Bell 2011; Widrow et al. 2011; Ryu et al. 2011, and references therein for recent reviews).

Secondly, we neglect the evolution of the spectrum of accelerated particles, and their energy losses via Coulomb and/or proton-proton collisions. The inclusion of losses may slightly decrease the amount of CRs inside our structures. However, for the densities typical of the structures of interest here this can be safely neglected, given that the time scales for significant energy losses of CR protons are large for typical non-cool core clusters (e.g. Miniati 2007; Pfrommer et al. 2007).

Thirdly, only direct shock acceleration is considered in this work as a channel to inject CRs in the cosmic gas. This is a safe enough assumption for most of the simulated volume, where the turbulent (e.g. Brunetti & Lazarian 2011b) and the shock (e.g. Blandford & Eichler 1987) re-acceleration of CRs should be neg-

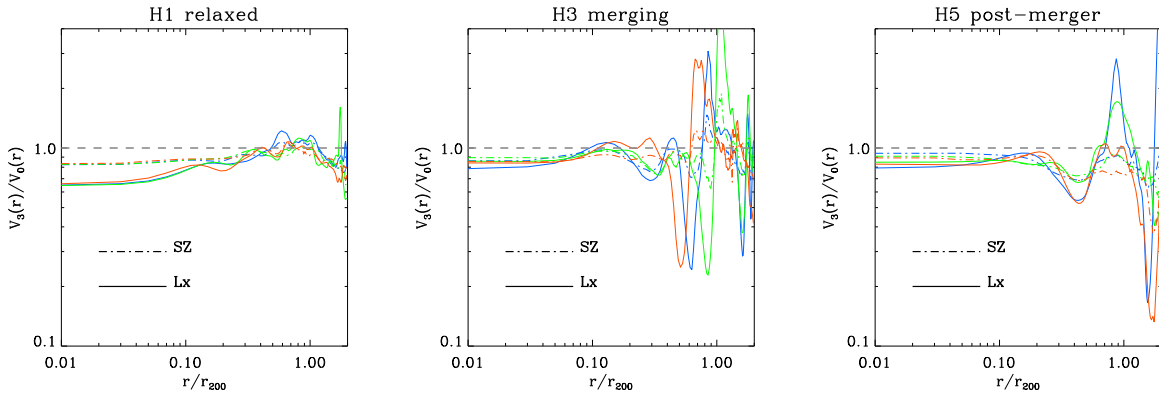


Figure 23. Radial average profile of the ratio between X-ray luminosity and SZ effect for re-simulations of clusters H1, H3 and H5 with (V3) and without (V0) CR physics. For each cluster, the radial trend for the 3 projections are shown in different colours.

ligible for the usually simple geometry of large-scale accretion pattern. In the centre of clusters, however, turbulence and shocklets structures can introduce also some significant re-acceleration of CRs. This additional channel of acceleration is not expected to boost CR energy ratio by more than a factor \sim a few over \sim Gyr time-scales. However, a future development of our method will also include these effects (and their feedback on the gas energy) in run-time. The injection of CRs at supernovae and AGN is also neglected in our model. Numerical studies using *GADGET* suggested that these additional CR sources are relevant only on very small ~ 10 kpc scales in proximity of the sources (Pfrommer et al. 2007). Heating of the thermal gas from the Alfvén waves excited by streaming of CRs (e.g. Guo & Oh 2008) is also an interesting physical process which can be incorporated in future work.

The description of the ICM in the runs presented here is simplified, since we neglected radiative cooling, and feedback from star formation and galactic activities, and magnetic fields. Radiative cooling can have an impact on the injection of CR energy at cold lumps of gas in the ICM (e.g. Pfrommer et al. 2007). However, the handling of cooling in simulations is still problematic since it produces strong (and un-observed) cooling flows in the inner regions of clusters, and it is still unclear how to quench them self-consistently. Magnetic field, even if not dynamical important, can be relevant to the study of CR energy in clusters because it affects the spatial propagation of CR (e.g. Hanasz & Lesch 2000; Jubelgas et al. 2008). However, for typical conditions in the ICM the scale-length of CR diffusion is smaller, or very close to, than our highest spatial resolution, 25 kpc/h (e.g. Blasi et al. 2007, and references therein), making our results still valid in a statistical sense.

Within the range of assumptions listed above, our method produces a number of interesting results with consequences on the modelling of galaxy clusters, and their comparison with observational data. Our runs at fixed mesh resolution show that the largest effect of CR feedback is concentrated at the outer accretion regions of cosmic structures, at over-densities close to the critical one (Sect.4.1). At $\rho/\rho_{\text{cr},b} \sim 1$ we measure $P_{\text{cr}}/P_g \sim 0.3 - 0.5$ on average. This result is very stable against all explored modifications of numerical parameters (the pressure ratio between CRs and gas for $\rho/\rho_{\text{cr},b} \leq 1$ is, on the other hand, significantly dependent on the assumed parameters). The use of AMR enables the investigation of the innermost region of galaxy cluster at a higher resolution (25 kpc/h). In this work we analysed 7 galaxy clusters with different dynamical states, in the range of total masses

$2 \cdot 10^{14} M_\odot \leq M \leq 1.1 \cdot 10^{15} M_\odot$ (Sect.4.2). We report a very low pressure ratio in the innermost cluster regions ($\leq 0.1 R_{200}$) is very small, $P_{\text{cr}}/P_g \sim 5 \cdot 10^{-3} - 3 \cdot 10^{-2}$, increasing up to a ~ 0.1 at R_{200} . No obvious dependence on cluster mass or dynamical state can be found in this small sample, except for the trend that dynamically perturbed systems display slightly larger values of P_{cr}/P_g , and tend to concentrate a significant amount of CR pressure in clumps of accreted sub-halos. In all systems, the effective adiabatic index of the mixture of gas and CRs is very close to the mono-atomic value of $\gamma = 5/3$ for $\leq 0.5 R_{200}$. In a few perturbed systems, however, it can be as small as $\gamma_{\text{eff}} \sim 1.6$ close to R_{200} .

It is important to compare the amount of CRs in our simulated clusters with available data from observations. A direct approach to constrain the energy content of CR protons in galaxy clusters is the observation of γ -ray emission from the decay of the neutral pions due to proton-proton collisions in the ICM. Gamma ray upper limits from *EGRET* observations allow to put limits of $E_{\text{cr}}/E_g < 0.3$ in several nearby galaxy clusters (Reimer et al. 2003). More stringent limits are derived from deep pointed observations at energies of > 100 GeV with Cherenkov telescopes. These limits depend on the (unknown) spectral shape of the proton-energy distribution. For the relevant case $\delta = 2$ (with $N(p) \propto p^{-\delta}$) the limits are $E_{\text{cr}}/E_g < 0.1$ (Aharonian et al. 2009; Aleksić et al. 2010), and they are less stringent for steeper spectra. Recently, the *FERMI* satellite greatly improved the sensitivity of observations at GeV energies, and the present upper limits for a large sample of nearby galaxy clusters are $E_{\text{cr}}/E_g < 0.05$ (e.g. Ackermann et al. 2010; Jeltema & Profumo 2011), with a poor dependence on δ . In addition to these methods, also the limits to the presence of diffuse Mpc-scale radio emission in clusters can be used to constrain secondary electrons and thus the energy density of the primary CR protons (Brunetti et al. 2007; Brown et al. 2011). In this case, the limits depend also on the cluster magnetic field strength and are complementary to those obtained from γ -rays. In the relevant case of an average magnetic field in cluster of a $\sim \mu\text{G}$, radio observations of clusters with no Mpc-scale radio emission suggest that $E_{\text{cr}}/E_g \leq 0.05$, while the limits are less stringent for smaller average magnetic fields. These limits usually refer to innermost \sim Mpc regions of clusters, where both the number density of thermal protons and the magnetic field are larger. At present no tight constraints are available for the clusters outskirts, where the CR contribution might be larger.

Given the mean value measured inside the innermost regions of all our re-simulated clusters (Sect.4.2), we conclude that at

present no obvious tension exists between the estimated energy budget of CRs injected at cosmological shock waves, at least for acceleration efficiencies in the range of those of Kang & Jones (2007). It is still possible that the inclusion of additional sources of CRs (as supernovae and AGN), as well as of re-acceleration from turbulence and shocks may increase the pressure of CRs close to available upper-limits. Therefore, in the next future a detailed comparison of γ -ray fluxes from secondary particles (possibly with more CR acceleration mechanisms) and observations will be important to address this topic more robustly.

When we compare the 3-D structure of the thermal gas in these clusters to their re-simulations which only employ standard non-radiative physics (Sec.4.2.1), we find small systematic trends: the innermost gas density, gas pressure and entropy at $z=0$ are a few percent smaller if feedback from CRs is considered, while they are larger by a similar amount at $\sim R_{200}$, leading to slightly flatter radial profiles. Based on our 1-D tests with the Zeldovich collapse (Sect.3.3) and also on specific re-simulations discussed in the Appendix A, we conclude that this arises from the time-integrated effect of having a lower γ_{eff} at the outer accretion regions of clusters. Accretion shocks are strong, $M \gg 10$, and their acceleration efficiency is large. CRs are accumulated here and they become dynamically important as the outer shells of matter of the structures expands with the growth of structures, because of their softer equation of state. This enhances the total pressure jump felt by infalling gas at $\sim R_{200}$ (while the gas pressure jump is slightly decreased by the effect of having a reduced thermalization efficiency), it increases the effective Mach number of the outer shocks, and it causes a slightly faster expansion of the outer shells compared to standard non-radiative runs (Sec.3.3). As a net effect, a few percent more gas matter is deposited in the outer regions, and a slightly less dense core is formed inside clusters. The reduced thermalization and the decreased gravitational potential in the innermost cluster regions also cause a smaller gas pressure, compared to simulations without CR feedback, by a few percent.

As we discussed in Sect.4.2.2, this feature has significant effects on the simulated properties of X-ray emission and SZ signal for our sample of clusters. When re-simulations with and without feedback from CR are compared, both signals are found to be decreased by a 10 – 30 percent in the innermost cluster regions ($\leq 0.1 R_{200}$) if CRs are accelerated, while they are increased by factors $\sim 0.5 – 4$ at R_{200} . The reported trends are found to be at variance with other ones based on SPH simulations (Pfrommer et al. 2007), where a significant boost of X-ray and SZ signal is reported for the innermost cluster regions. To our understanding these differences can be totally ascribed to the fundamental differences in the way the two numerical approaches model at a run-time the accretion of gas satellites, their entropy enrichment and their stripping into the main cluster atmosphere. This problem is related to the more fundamental ones of artificial viscosity and pre-shock entropy generation in SPH (e.g. Agertz et al. 2007; Wadsley et al. 2008; Mitchell et al. 2009; Vazza 2011; Vazza et al. 2011b; Sijacki et al. 2011, and references therein).

6 CONCLUSIONS

In this work we presented our numerical implementation of cosmic ray injection, advection and feedback in cosmological simulations with the ENZO code. Our method incorporates a prescription for Diffusive Shock Acceleration (e.g. Bell 1978; Drury & Voelk

1981; Kang & Jones 2007), and channels at run-time energy from the thermal gas to the CR pool, thus reducing the post-shock thermal energy flux. The main step of our algorithm are the following: a) in run-time we measure the 3-D distribution of Mach number using a shock finder based on pressure jumps; b) we estimate the total energy flux of CR protons as a function of Mach number, assuming an acceleration efficiency from theoretical models (in our case, Kang & Jones 2007); c) we update the energy of CR energy within each shocked cell, and we advect CR energy assuming no diffusion of CRs, for a fixed adiabatic index of $\gamma_{\text{cr}} = 4/3$; d) we feed the total pressure, $P_g + P_{\text{cr}}$ (rather than the simple gas pressure, as in standard runs) into the Riemann solver. Therefore, the composite fluid of gas and CRs in the simulation follows an effective adiabatic index, $\gamma_{\text{eff}} \leq \gamma = 5/3$, depending on the local energy ratio between CRs and the gas energy within the cells.

We tested our method in simple 1-D tests (Sec.3), finding good agreement with analytical estimates for shock-tube tests. The role of the various parameters involved in the injection and advection of CRs was tested separately with shocks of different strength (Sec.3.2). The cosmological application of our method for CRs was studied in 1-D using the Zeldovich pancake collapse test, where also the use of adaptive mesh refinement was tested (Sec.3.3).

We studied the injection and the evolution of CRs in large-scale structures with cosmological simulations at fixed grid resolution (Sec.4.1) and with adaptive mesh refinement (Sec.4.2). For fixed grid runs, we report an increase in the total CPU time of the order of $\sim 10 – 20$ percent compared to standard non-radiative runs. These low and moderate resolution runs were used to estimate the large-scale properties of CRs in the cosmic volume, and to test the robustness of our findings against a number of assumptions. The level of CR energy inside cosmic structures is found to be small, $P_{\text{cr}}/P_g \leq 0.1$, with a peak at the over-density typical of outer accretion regions. We report that only the distribution of CRs outside of cosmic structures is strongly dependent on the details involved in the acceleration in the early cosmic epochs (and in the most rarefied environments) while the distributions of CRs are very stable for the innermost regions of clusters.

Using adaptive mesh refinement we investigated the properties of 7 galaxy clusters, with masses in the range $2.1 \cdot 10^{14} M_{\odot} \leq M \leq 1.5 \cdot 10^{15} M_{\odot}$, and different dynamical states. The dynamical role of accelerated CR energy is always quite small, and plays a significant dynamical role only close to $\sim R_{200}$. In the centre of clusters instead the pressure of CRs is small, $P_{\text{cr}}/P_g \sim 0.02 – 0.05$. These values are presently consistent with the upper-limits provided from γ -ray observations (Sec.5).

The effects of CRs on the overall evolution of clusters have small and systematic effects on the 3-D distribution of the thermal baryonic gas. In all re-simulated clusters in the innermost gas density, temperature and entropy are reduced by a few percent, while they are enhanced on average by the same amount at R_{200} (Sec.4.2). This comes from the fact that CRs first modify the compressibility of outer accretion regions during the formation of structures, leading to an enhanced post-shock compression and to a slightly faster expansion of the outer cluster layers compared to standard simulations. This produces also a corresponding decrease of X-ray emission and of the thermal SZ signal from the inner cluster region, and an enhancement of a factor $\sim 0.4 – 4$ close to R_{200} , and depending of the dynamical state of the clusters (Sec.4.2.2).

These systematic trends in galaxy clusters are at variance with results obtained with SPH for qualitatively similar treatment of CRs dynamics (Pfrommer et al. 2007; Jubelgas et al. 2008), where en-

hanced gas density is found in cluster cores, and unchanged gas distributions are measured further out. The reason of these differences is not clear. We conjecture that the most likely explanation lies in the different way in which transport and mixing motions are modelled in grid methods and in SPH, leading to a more efficient large-scale mixing of injected CRs in Eulerian runs. This would be in line with recent comparisons performed by our group on simple non-radiative cosmological simulations using and ENZO and GADGET (Vazza et al. 2011b). Performing similar comparisons in cosmology, and with the inclusion of CRs physics, is a necessary next step to study non-thermal processes in cosmology.

To summarize, the first step for incorporating particle acceleration at shocks in run-time in ENZO, and the physical feedback of CRs on the baryon gas is successful for the ensemble of tests and cosmological simulations we explored. To our knowledge, this is the first time that such studies are successfully performed for cosmological simulations with adaptive mesh refinement, and for realistic models of shock acceleration and reduced thermalization. This model enables us to explore non-thermal phenomena in galaxy clusters, and to take advantage of the capabilities of the PPM method to model turbulence and shocks in the simulated intra cluster medium. The inclusion of more complex treatment of CR dynamics (e.g. using spectral energy bins, Miniati 2007), as well as the porting of these methods to more sophisticated and recent development of ENZO (e.g. Collins et al. 2010) are under way, and will allow us to simulate the non-thermal features of the ICM with unprecedented detail.

ACKNOWLEDGEMENTS

F.V. and M.B. acknowledge support from the grant FOR1254 from the Deutsche Forschungsgemeinschaft. F.V. acknowledges the usage of computational resources under the CINECA-INAF 2008-2010 agreement, and at the John-Neumann Institut at the Forschungszentrum Jülich. G.B. acknowledges partial financial support from PRIN-INAF 2009 and ASI-INAF I/009/10/0. We are grateful to S. Rösswog for his help in the 1-D tests of the code, to J. Favre for his support in the use of *VISIT*. We gratefully acknowledge the ENZO development group for providing helpful on-line documentations and tutorials (<http://lca.ucsd.edu/software/enzo/>).

REFERENCES

- Abel T., Anninos P., Norman M. L., Zhang Y., 1998, ApJ, 508, 518
- Ackermann M. et al., 2010, ApJL, 717, L71
- Agertz O. et al., 2007, MNRAS, 380, 963
- Aharonian F. et al., 2009, ApP, 495, 27
- Aleksić J. et al., 2010, ApJ, 710, 634
- Amato E., Blasi P., 2005, MNRAS, 364, L76
- Bautz M. W. et al., 2009, Publications of the Astronomical Society of Japan, 61, 1117
- Bell A. R., 1978, MNRAS, 182, 147
- Berezinsky V. S., Blasi P., Ptuskin V. S., 1997, ApJ, 487, 529
- Berger M. J., Colella P., 1989, Journal of Computational Physics, 82, 64
- Blandford R., Eichler D., 1987, Physical Reports, 154, 1
- Blandford R. D., Ostriker J. P., 1978, ApJL, 221, L29
- Blasi P., 2004, Nuclear Physics B Proceedings Supplements, 136, 208
- Blasi P., Colafrancesco S., 1999, Astropart. Phys., 122, 169
- Blasi P., Gabici S., Brunetti G., 2007, International Journal of Modern Physics A, 22, 681
- Bonafede A., Dolag K., Stasyszyn F., Murante G., Borgani S., 2011, ArXiv e-prints
- Brown S., Emerick A., Rudnick L., Brunetti G., 2011, ApJL, 740, L28
- Brüggen M., Bykov A., Ryu D., Röttgering H., 2011, Science & Space Review, 71
- Brunetti G. et al., 2008, Nature, 455, 944
- Brunetti G., Lazarian A., 2011a, MNRAS, 410, 127
- Brunetti G., Lazarian A., 2011b, MNRAS, 412, 817
- Brunetti G., Venturi T., Dallacasa D., Cassano R., Dolag K., Giacintucci S., Setti G., 2007, ApJL, 670, L5
- Bryan G. L., Norman M. L., Stone J. M., Cen R., Ostriker J. P., 1995, Computer Physics Communications, 89, 149
- Bykov A. M., Bloemen H., Uvarov Y. A., 2000, ApP, 362, 886
- Caprioli D., Kang H., Vladimirov A. E., Jones T. W., 2010, MNRAS, 407, 1773
- Carilli C. L., Taylor G. B., 2002, ARAA, 40, 319
- Colella P., Woodward P. R., 1984, Journal of Computational Physics, 54, 174
- Collins D. C., Xu H., Norman M. L., Li H., Li S., 2010, ApJS, 186, 308
- Dolag K., Bartelmann M., Lesch H., 1999, ApP, 348, 351
- Dolag K., Bykov A. M., Diaferio A., 2008, Science & Space Review, 134, 311
- Dolag K., Enßlin T. A., 2000, ApP, 362, 151
- Donnert J., Dolag K., Lesch H., Müller E., 2009, MNRAS, 392, 1008
- Drury L. O., Voelk J. H., 1981, ApJ, 248, 344
- Eckert D., Molendi S., Gastaldello F., Rossetti M., 2011a, ApP, 529, A133
- Eckert D. et al., 2011b, ArXiv e-prints
- Edmon P. P., Kang H., Jones T. W., Ma R., 2011, MNRAS, 414, 3521
- Ellison D. C., Baring M. G., Jones F. C., 1995, ApJ, 453, 873
- Enßlin T. A., Pfrommer C., Springel V., Jubelgas M., 2007, ApP, 473, 41
- Ferrari C., Govoni F., Schindler S., Bykov A. M., Rephaeli Y., 2008, Science & Space Review, 134, 93
- Gargaté L., Spitkovsky A., 2011, ArXiv e-prints
- George M. R., Fabian A. C., Sanders J. S., Young A. J., Russell H. R., 2009, MNRAS, 395, 657
- Gheller C., Pantano O., Moscardini L., 1998, MNRAS, 296, 85
- Godunov S. K., Zabrodin A. V., Ivanov M. I., Kraiko A. N., Prokopov G. P., 1976, Moscow Izdatel Nauka
- Govoni F., Feretti L., Giovannini G., Dallacasa D., Taylor G. B., 2002, in M. Gilfanov, R. Sunyaev, & E. Churazov , ed, Light-houses of the Universe: The Most Luminous Celestial Objects and Their Use for Cosmology, p. 78
- Guo F., Oh S. P., 2008, MNRAS, 384, 251
- Haardt F., Madau P., 1996, ApJ, 461, 20
- Hallman E. J., Motl P. M., Burns J. O., Norman M. L., 2006, ApJ, 648, 852
- Hanasz M., Lesch H., 2000, ApJ, 543, 235
- Hockney R., Eastwood J., 1988, Computer simulation using particles. Bristol: Hilger, 1988
- Hoeft M., Brüggen M., Yepes G., Gottlöber S., Schwabe A., 2008, MNRAS, 391, 1511
- Iapichino L., Niemeyer J. C., 2008, MNRAS, 388, 1089
- Jeltema T. E., Profumo S., 2011, ApJ, 728, 53

- Jubelgas M., Springel V., Enßlin T., Pfrommer C., 2008, ApP, 481, 33
- Kang H., Jones T. W., 1990, ApJ, 353, 149
- Kang H., Jones T. W., 2007, Astroparticle Physics, 28, 232
- Kang H., Ryu D., 2010, ApJ, 721, 886
- Kang H., Ryu D., Cen R., Ostriker J. P., 2007, ApJ, 669, 729
- Kang H., Ryu D., Jones T. W., 2009, ApJ, 695, 1273
- Malkov M. A., O'C Drury L., 2001, Reports on Progress in Physics, 64, 429
- Mathews W. G., Brighenti F., 2007, ApJ, 660, 1137
- Mathews W. G., Guo F., 2011, ApJ, 736, 6
- Miniati F., 2007, Journal of Computational Physics, 227, 776
- Miniati F., Bell A. R., 2011, ApJ, 729, 73
- Miniati F., Jones T. W., Kang H., Ryu D., 2001, ApJ, 562, 233
- Miniati F., Ryu D., Kang H., Jones T. W., Cen R., Ostriker J. P., 2000, ApJ, 542, 608
- Mitchell N. L., McCarthy I. G., Bower R. G., Theuns T., Crain R. A., 2009, MNRAS, 395, 180
- Norman M. L., Bryan G. L., Harkness R., Bordner J. a., 2007, ArXiv e-prints, 705
- O'Shea B. W., Bryan G., Bordner J., Norman M. L., Abel T., Harkness R., Kritsuk A., 2004, ArXiv Astrophysics e-prints
- Pfrommer C., Enßlin T. A., Springel V., Jubelgas M., Dolag K., 2007, MNRAS, 378, 385
- Pfrommer C., Springel V., Enßlin T. A., Jubelgas M., 2006, MNRAS, 367, 113
- Pierre M., Pacaud F., Juin J. B., Melin J. B., Valageas P., Clerc N., Corasaniti P. S., 2011, MNRAS, 414, 1732
- Pinzke A., Pfrommer C., 2010, MNRAS, 409, 449
- Reimer O., Pohl M., Sreekumar P., Mattox J. R., 2003, ApJ, 588, 155
- Reynolds S. P., 2008, ARAA, 46, 89
- Roncarelli M., Ettori S., Dolag K., Moscardini L., Borgani S., Murante G., 2006, MNRAS, 373, 1339
- Ruszkowski M., Lee D., Brüggen M., Parrish I., Oh S. P., 2011, ApJ, 740, 81
- Ruszkowski M., Oh S. P., 2011, MNRAS, 414, 1493
- Ryu D., Kang H., 2004, Journal of Korean Astronomical Society, 37, 477
- Ryu D., Kang H., Biermann P. L., 1998, ApP, 335, 19
- Ryu D., Kang H., Hallman E., Jones T. W., 2003, ApJ, 593, 599
- Ryu D., Ostriker J. P., Kang H., Cen R., 1993, ApJ, 414, 1
- Ryu D., Schleicher D. R. G., Treumann R. A., Tsagas C. G., Widrow L. M., 2011, ArXiv e-prints
- Sijacki D., Vogelsberger M., Keres D., Springel V., Hernquist L., 2011, ArXiv e-prints
- Simionescu A. et al., 2011, Science, 331, 1576
- Skillman S. W., O'Shea B. W., Hallman E. J., Burns J. O., Norman M. L., 2008, ApJ, 689, 1063
- Springel V., 2005, MNRAS, 364, 1105
- Tasker E. J., Brunino R., Mitchell N. L., Michielsen D., Hopton S., Pearce F. R., Bryan G. L., Theuns T., 2008, MNRAS, 390, 1267
- Urban O., Werner N., Simionescu A., Allen S. W., Böhringer H., 2011, MNRAS, 414, 2101
- Vazza F., 2011, MNRAS, 410, 461
- Vazza F., Brunetti G., Gheller C., 2009, MNRAS, 395, 1333
- Vazza F., Brunetti G., Gheller C., Brunino R., 2010, New Astronomy, 15, 695
- Vazza F., Brunetti G., Gheller C., Brunino R., Brüggen M., 2011a, ApP, 529, A17
- Vazza F., Brunetti G., Kritsuk A., Wagner R., Gheller C., Norman M., 2009, ApP, 504, 33
- Vazza F., Dolag K., Ryu D., Brunetti G., Gheller C., Kang H., Pfrommer C., 2011b, ArXiv e-prints
- Vazza F., Gheller C., Brunetti G., 2010, ApP, 513, A32
- Vazza F., Roncarelli M., Ettori S., Dolag K., 2011c, MNRAS, 413, 2305
- Vink J., Yamazaki R., Helder E. A., Schure K. M., 2010, ApJ, 722, 1727
- Völk H. J., Atoyan A. M., 1999, Astroparticle Physics, 11, 73
- Wadsley J. W., Veeravalli G., Couchman H. M. P., 2008, MNRAS, 387, 427
- Widrow L. M., Ryu D., Schleicher D., Subramanian K., Tsagas C. G., Treumann R. A., 2011, ArXiv e-prints
- Zweibel E. G., Heitsch F., 2008, ApJ, 684, 373

APPENDIX A: INVESTIGATING THE REASON OF A LOWER CENTRAL DENSITY

In this Section we present a numerical test designed to highlight the impact of CR physics on the formation of galaxy clusters, at an early stage of their assembly. In this test, we selected a cubic sub-volume of side 10 Mpc/h around the forming cluster H3 at $z=2$. This is a standard non-radiative run in the redshift range $30 \geq z > 2$. Starting from $z = 2$, we evolve two re-simulations of the same volume, allowing CRs injection and feedback in the first, and following standard non-radiative physics in the second. At each root-grid time step ($\Delta t \sim 0.05$ Myr) we compare the thermal properties of gas halos in the two runs. This highlights the timely role of CRs in our runs, which is responsible of the significant differences discussed in Sect.4.2. In the first three panels of Fig.A1 we show the time-sequence of profiles for the normalized difference of gas density, gas pressure and total pressure for a massive halo in our sample ($M \sim 4 \cdot 10^{13} M_\odot$ at $z=2$). In detail, we compute $(V_{\text{cr}}(R) - V_0(R))/V_0(R)$, where $V_{\text{cr}}(R)$ is the profile of each quantity in the run with CRs feedback, and $V_0(R)$ is the corresponding profile in the run with no CRs feedback. The last three panels of the same Figure report the time evolution of CR pressure, pressure ratio and γ_{eff} for the re-simulation with CRs feedback.

The injection of CRs within halos starts mainly from outer accretion shocks (at ~ 0.2 Mpc/h in the Figure), and at internal merger shocks at the centre of the structure. The energy feedback of CRs is initially more important in the outer proto-cluster regions (since the Mach number is large here), leading to a small and continuous decrease of the effective adiabatic index of the mixture of gas and CRs. The gas pressure in the run with CRs after a few time-steps is initially reduced by a $\sim 1 - 2$ percent, while the total pressure remains almost constant. The post-shock gas density at the outer regions is progressively increased by the enhanced compressibility at the shock. This in turn leads to a smaller deposition of gas matter (reducing gas density by ~ 1 percent) at the outer cluster parts, compared to the standard run. The outer shells expand into the rarefying cosmic volume, and the smaller adiabatic index of CR energy makes it even more dynamically important as the expansion goes on. By the end of our test ($z \approx 1.6$) this has caused the increase of ~ 5 percent in the total (gas+CR) pressure at the outer proto-cluster regions. We thus expect that shock waves are slightly stronger at $\sim R_{200}$ in the run with CRs, even at later times. This makes the injection of new CRs an even more efficient process, and

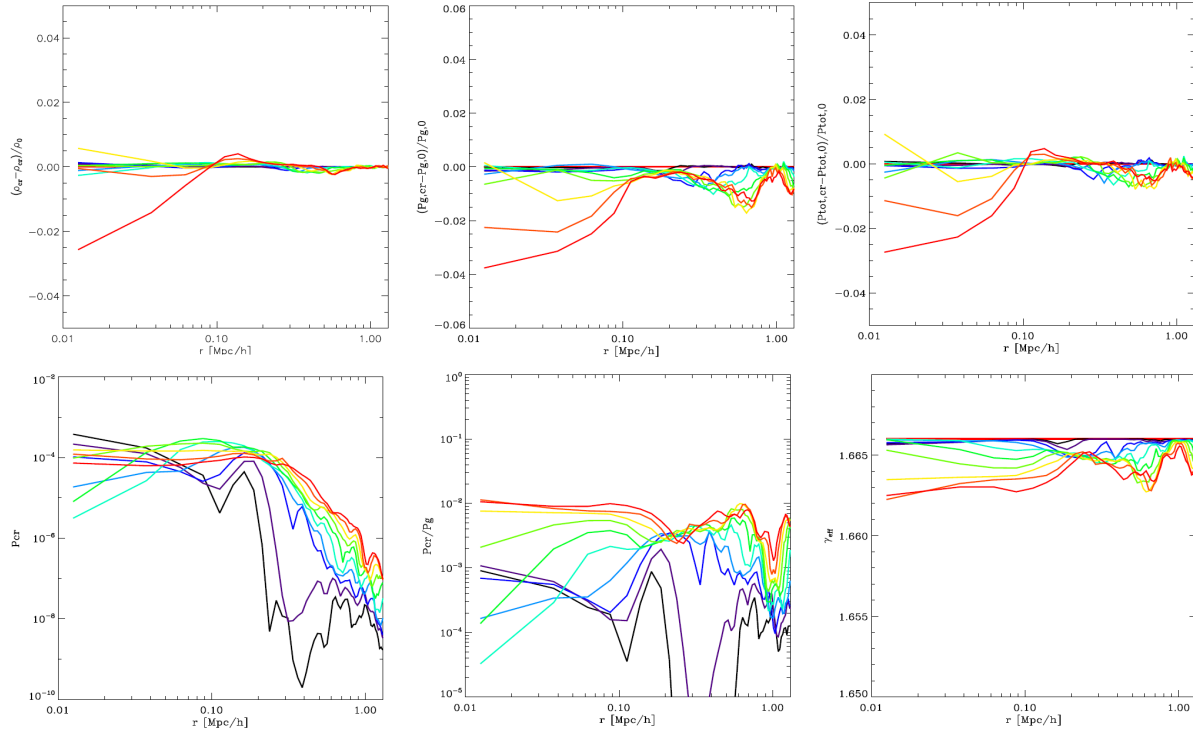


Figure A1. First three panels: time evolution of the ratio of gas density, gas pressure and total pressure in a re-simulated halos of run H3 with and without CR physics. Last three panels: time evolution of the CRs pressure, pressure ratio and effective adiabatic index for the same cluster. The injection of CR has been started at $z=2$ in this case. The time sequence goes from blue to green to red colours, the time lag between each profile is $\Delta t \sim 0.05$ Gyr.

maintains the difference with standard runs even at later times, as observed in our clusters at $z=0$ (Sect.4.2).